X-shaped Radical Offshore Wind Turbine for Overall Cost of Energy Reduction

D2.1

# Aero-elastic dynamic model capable of modelling the X-ROTOR

https://xrotor-project.eu

@XROTORProject

**January 2021**

This project has received funding from the European Union's Horizon 2020 research and innovation programme under grant agreement No 101007135

# Project Coordinator Approval Form

Project acronym: **XROTOR**
Grant agreement number: 101007135
Start date: 01st January 2021
Duration: 3 years

*Document Information*

| Date | Description | Prepared by | Reviewed by | Approved by |
|---|---|---|---|---|
| 30/01/2021 | Final version | Carlos Ferreira | W. Leithead & J. Carroll | W. Leithead (Project Coordinator) |

The X-ROTOR Project has received funding from the European Union's Horizon 2020 research and innovation programme under grant agreement no. 101007135. For more information on the project, its partners, and contributors please see https://XROTOR-project.eu.

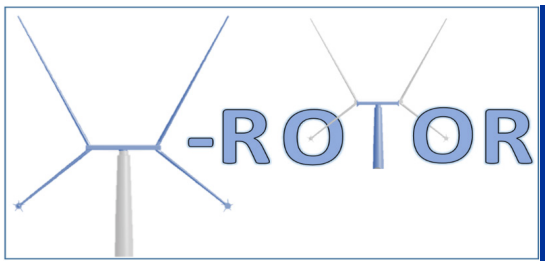


# X-ROTOR: X-shaped Radical Offshore wind Turbine for Overall cost of energy Reduction

*Work Package WP2*

## Aero-elastic code development and performance

*Deliverable D2.1*

## Aero-elastic dynamic model capable of modelling the X-Rotor

| | |
|---|---|
| *Funding Instrument:* | Innovation Action |
| *Call:* | H2020-LC-SC3-2018-2019-2020 |
| *Call Topic:* | LC-SC3-RES-1-2019-2020 |
| *Project Start:* | 1 January 2021 |
| *Project Duration:* | 36 months |
| *Beneficiary in Charge:* | TU Delft |

| Dissemination Level | | |
|---|---|---|
| PU | Public | ✓ |
| PP | Restricted to other programme participants (including the Commission Services) | |
| RE | Restricted to a group specified by the Consortium (including the Commission Services) | |
| CO | Confidential, only for members of the Consortium (including the Commission Services) | |

## Deliverable Information

| Document Administrative Information | |
|---|---|
| Project Acronym: | XROTOR |
| Project Number: | 101007135 |
| Deliverable Number: | D2.1 |
| Deliverable Full Title: | Aero-elastic dynamic model capable of modelling the X-Rotor |
| Deliverable Short Title: | XROTOR aeroelastic model |
| Document Identifier: | XROTOR-D21-XROTORAeroelasticModel-submitted |
| Beneficiary in Charge: | TU Delft |
| Report Version: | v1.1 |
| Contractual Date: | 30/09/2021 |
| Report Submission Date: | 30/09/2021 |
| Dissemination Level: | PU |
| Nature: | Report |
| Lead Author(s): | Prof. Carlos Ferreira (TUDelft) |
| Co-author(s): | Bruce LeBlanc (while at TUDelft) |
| Keywords: | Aeroelastic model, Actuator Cylinder model, aerodynamic loads |
| Status: | __ draft, __ final, _x_ submitted |

## Document information

| Date | Version | Author/Editor | Summary of Changes Made |
|---|---|---|---|
| 29/09/2021 | v1.0 | Prof. Carlos Ferreira (TU Delft) | Draft version of the report |
| 30/09/2021 | v1.1 | Prof. Carlos Ferreira (TU Delft) | Reviewed for confidentiality and cleared for submission. Reviewers: Prof. W. Leithead, Dr. James Carroll, David Bensason, Adhyanth Giri Ajay |
| | | | |

# Table of Contents

# List of Figures

# List of Tables

# Executive Summary

## 0.1 Deliverable Description

The deliverable is described in the project proposal as *D2.1: Aero-elastic dynamic model capable of modelling the X-Rotor (M9)*. This is the first deliverable of *Task 2.1: Create Aero-Elastic Dynamic Modelling tool*.

## 0.2 Responsible:

The responsible partner is TU Delft, with Prof. Carlos Ferreira as principal investigator.

## 0.3 Outcome Summary:

The current version of the Aero-Elastic Dynamic Modelling tool, as described in this report, is able to (text from the description of Task 2.1 *in italic*):

- model *the complex geometry of the X-Rotor* (primary rotor)
- assess *the deformations of the blades under unsteady loading and the effect of localised forces due to the small rotors.*
- simulate *the unsteady aerodynamics of the rotor*.
- structurally model the rotor with *linear beam elements*.
- be coupled to an *aerodynamic model for VAWTs: an actuator cylinder model, for fast load simulation*.

The aeroelastic model has been validated using wind tunnel data from a VAWT.

The aerodynamic model was used to calculate the loads and performance of the X-Rotor's primary rotor. The data is uploaded along with the report and distributed to project partners. This document also supports the shared simulation results database. The outcomes include normal operational conditions as well as extreme loads in stand-still situations.

The source code and simulation files will be made available upon request for the duration of the X-Rotor project, and made available in an open repository upon conclusion of the project.

The model can support the X-Rotor project's immediate planned activities. As described in Task 2.1, the model will be further developed in the project, both as part of Task 2.1 and in conjunction with other tasks.

# 1 Deliverable details

This report supports deliverable *D2.1 Aero-elastic dynamic model capable of modelling the X-Rotor*. It describes the implementation of the aero-elastic model in its current form and supports a shared database of simulation results of the aerodynamic performance of the X-Rotor's primary rotor (including loads), assuming a rigid rotor and no secondary rotor.

The document is organised as follows: Section 2 presents the key formulation of the 2D Actuator Cylinder model used for the simulation of the XRotor. Section 4 describes the rotor and operational conditions (Section 4.1) and presents the results for rotor performance and stand-still loading cases. Section 5 discusses the relevance of the results for the X-Rotor project and next steps. Appendix A - Definition of the output file with load distribution describes the files of the database of simulation results of the aerodynamic performance of the X-Rotor's primary rotor (including loads). Appendix B - Airfoil polars presents the airfoil polars considered in this study.

# 2 Deliverable Outcome: aerodynamic model

This section presents the theoretical description of the aerodynamic model used for the simulation of the X-Rotor.

The capacity to generate force fields over actuator surfaces that interchange momentum and energy with the fluid is critical for energy conversion from wind and water, as well as aviation and ship propulsion. Rotors that approximate the ideal actuation surface, such as horizontal axis wind turbines and propellers, are commonly used to generate an actuator disc (see (Glauert, 1948), (G. van Kuik, 2018) and (G. A. van Kuik, 2020), and (Madsen, 1988) for an arbitrary rotor shape). As an approximation of the 3D Actuator Cylinder, the Vertical Axis Wind Turbine (VAWT) and Propeller generate a force field over a circular surface.

The revolution of actuator elements such as blades, struts, and towers characterize these surfaces. The 3D design space yields a wide range of rotor shapes (Figure 1) that represent cylindrical surfaces; their diameter can vary with height and they can have varying height to diameter aspect ratios. The surface can also be a combination of nested and/or crossing revolution surfaces, such as those generated by the blades and struts. The loading on the 3D Actuator Cylinder will vary in height/spanwise and azimuthal direction (perpendicular to the plane of rotation).

Due to the complexity of the 3D Actuator Cylinder, the analysis of VAWTs has relied on dividing the 3D actuator cylinder in 2D actuator cylinders that are stacked up in height (see (Larsen & Madsen, 2013) and (Keijer, 2020)). This approach relies on the assumption of streamtube independence as used in actuator disc theory in axial flow ((G. van Kuik, 2018)). For the 3D Actuator Cylinder the streamtubes are not independent in any direction and the assumption is incorrect and leads to significant errors (see (Simao Ferreira & Scheurich, 2014), (Ferreira et al., 2014) and (Simao Ferreira, 2009) ). H. Madsen created the 2D actuator cylinder model (Madsen, 1983). It employs a two-dimensional formulation of the momentum equations that allows for the use of a linearized form of the equations. The external force field is required as input for the actuator cylinder model. An iterative approach with a blade element model is frequently used for this: (1) use the blade element model to determine the force field from the velocity field outputted from the actuator cylinder model; (2) use the actuator cylinder model to determine the flow field from the force field outputted from the blade element model.

## 2.1 Equations for the 3D Actuator Cylinder

The 3D Actuator Cylinder is a 3D formulation of the momentum equations that favours the application of a linearised form of the equations. The formulation used in this work is adapted from the derivation presented by von Kármán and Burgers in Chapter III, Section 6 of the book *Aerodynamic Theory* edited by (Durand, 1935) and is inspired by the work of (Madsen, 1983) and (Madsen, 1988).

Assuming that the flow is 3D, and that the main flow direction is in x-direction $U_\infty$, the velocity $\vec{v}$ can be defined in Cartesian coordinates by perturbations in relation to the unperturbed flow $U_\infty$ as

$$\vec{v} = \begin{bmatrix} 1 + u_x \\ u_y \\ u_z \end{bmatrix} U_\infty \tag{1}$$

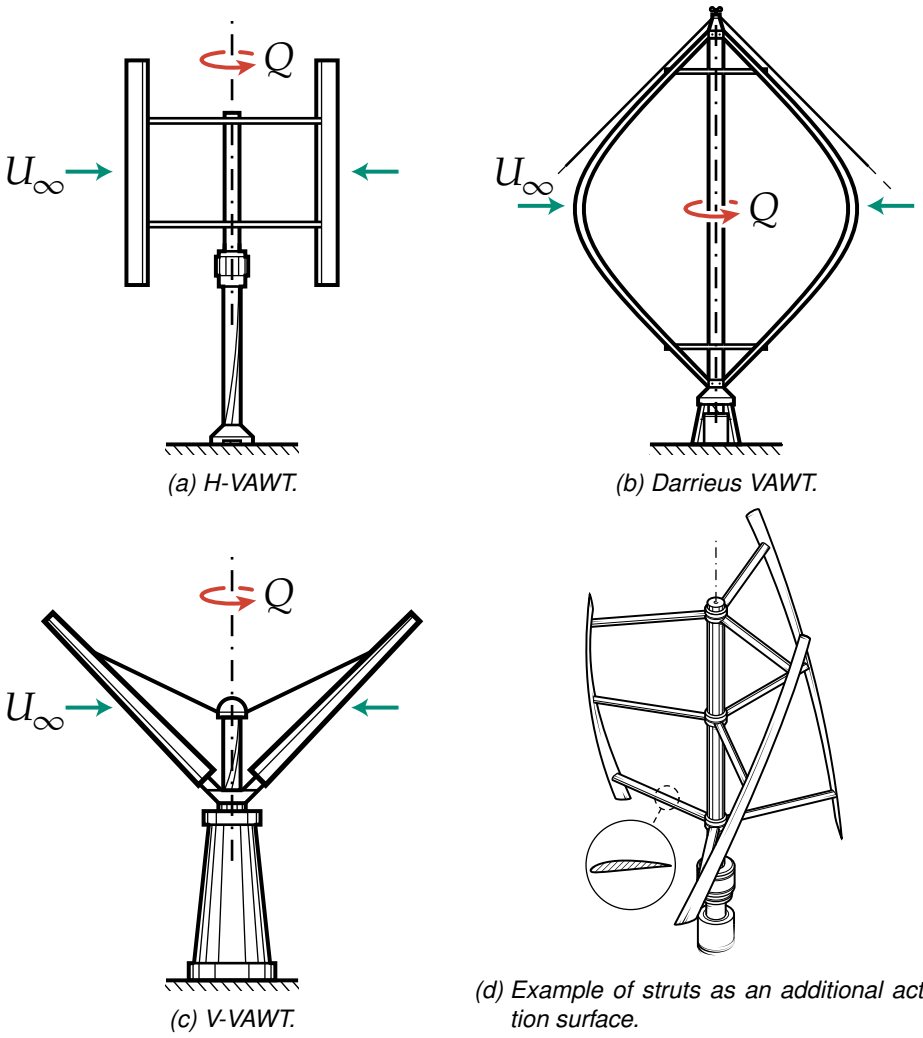


(a) H-VAWT.

(b) Darrieus VAWT.

(c) V-VAWT.

(d) Example of struts as an additional actuation surface.

*Figure 1: Examples of different VAWT rotor configurations which generate different actuation surfaces (images by R. Bos, with permission)*

where $[u_x, u_y, u_z]$ are non-dimensional perturbations terms.

As $U_\infty$ is constant, the steady, incompressible and inviscid 3D momentum and continuity equations can be simplified as:

$$\frac{\partial u_x}{\partial x} + u_x\frac{\partial u_x}{\partial x} + u_y\frac{\partial u_x}{\partial y} + u_z\frac{\partial u_x}{\partial z} = -\frac{\partial p}{\partial x}\frac{1}{\rho U_\infty^2} + f_x\frac{1}{\rho U_\infty^2} \tag{2}$$

$$\frac{\partial u_y}{\partial x} + u_x\frac{\partial u_y}{\partial x} + u_y\frac{\partial u_y}{\partial y} + u_z\frac{\partial u_y}{\partial z} = -\frac{\partial p}{\partial y}\frac{1}{\rho U_\infty^2} + f_y\frac{1}{\rho U_\infty^2} \tag{3}$$

$$\frac{\partial u_z}{\partial x} + u_x\frac{\partial u_z}{\partial x} + u_y\frac{\partial u_z}{\partial y} + u_z\frac{\partial u_z}{\partial z} = -\frac{\partial p}{\partial z}\frac{1}{\rho U_\infty^2} + f_z\frac{1}{\rho U_\infty^2} \tag{4}$$

$$\frac{\partial u_x}{\partial x} + \frac{\partial u_y}{\partial y} + \frac{\partial u_z}{\partial z} = 0 \tag{5}$$

where $[f_x, f_y, f_z]$ are external force terms. Using vector identity, we will first rearrange the second order terms as, for example in the $x$-direction:

$$u_x\frac{\partial u_x}{\partial x} + u_y\frac{\partial u_x}{\partial y} + u_z\frac{\partial u_x}{\partial z} = \frac{\partial}{\partial x}\left(\frac{u_x^2+u_y^2+u_z^2}{2}\right) + \frac{\omega_y u_z}{U_\infty^2} - \frac{\omega_z u_y}{U_\infty^2} \tag{6}$$

where $[\omega_x, \omega_y, \omega_z]$ is the vorticity in $x$, $y$ and $z$ directions, respectively.

We can rewrite the momentum equations by moving all the terms that are of second degree in the perturbation quantities to the right side.

$$\frac{\partial u_x}{\partial x} = -\frac{\partial p}{\partial x}\frac{1}{\rho U_\infty^2} - \frac{\partial}{\partial x}\left(\frac{u_x^2+u_y^2+u_z^2}{2}\right) + f_x\frac{1}{\rho U_\infty^2} - \frac{\omega_y u_z}{U_\infty^2} + \frac{\omega_z u_y}{U_\infty^2} \tag{7}$$

$$\frac{\partial u_y}{\partial x} = -\frac{\partial p}{\partial y}\frac{1}{\rho U_\infty^2} - \frac{\partial}{\partial y}\left(\frac{u_x^2+u_y^2+u_z^2}{2}\right) + f_y\frac{1}{\rho U_\infty^2} - \frac{\omega_z u_x}{U_\infty^2} + \frac{\omega_x u_z}{U_\infty^2} \tag{8}$$

$$\frac{\partial u_z}{\partial x} = -\frac{\partial p}{\partial z}\frac{1}{\rho U_\infty^2} - \frac{\partial}{\partial z}\left(\frac{u_x^2+u_y^2+u_z^2}{2}\right) + f_z\frac{1}{\rho U_\infty^2} - \frac{\omega_x u_y}{U_\infty^2} + \frac{\omega_y u_x}{U_\infty^2} \tag{9}$$

$$\tag{10}$$

We now define a quantity $q$ as:

$$q = p + \rho\frac{u_x^2+u_y^2+u_z^2}{2}U_\infty^2 - p_0 \tag{11}$$

where $p_0$ is the unperturbed pressure at infinity, which is constant.

The equations can be rewritten in the form:

$$\begin{aligned}
\frac{\partial u_x}{\partial x} &= -\frac{\partial q}{\partial x}\frac{1}{\rho U_\infty^2} + f_x\frac{1}{\rho U_\infty^2} + g_x\frac{1}{\rho U_\infty^2} \\
\frac{\partial u_y}{\partial x} &= -\frac{\partial q}{\partial y}\frac{1}{\rho U_\infty^2} + f_y\frac{1}{\rho U_\infty^2} + g_y\frac{1}{\rho U_\infty^2} \\
\frac{\partial u_z}{\partial x} &= -\frac{\partial q}{\partial z}\frac{1}{\rho U_\infty^2} + f_z\frac{1}{\rho U_\infty^2} + g_z\frac{1}{\rho U_\infty^2}
\end{aligned} \tag{12}$$

where:

$$g_x = \rho\left(u_y\omega_z - u_z\omega_y\right) \tag{13}$$
$$g_y = \rho\left(u_z\omega_x - u_x\omega_z\right) \tag{14}$$
$$g_z = \rho\left(u_x\omega_y - u_y\omega_x\right) \tag{15}$$

The system of Equations 12 is an exact representation of fluid motion of a steady, incompressible and inviscid fluid. On the other hand, if we neglect the nonlinear terms $g_{x,y,z}$, the solution is a first approximation of the flow field. The terms of vorticity in this system of equations are then treated as a "force term" and sometimes named "induced forces". For actuator discs with significant loading, these $g_{x,y,z}$ terms are significant. We will call the solution where these "induced forces" are neglected as the "linear solution". An iterative approach can be used to achieve the full solution while starting from the linear solution (see (Durand, 1935)). However, we will for now focus on the linear solution. In addition, engineering corrections can be applied to the linear solution and improve its approximation of the full solution (see Section 2.3).

By taking the divergence of the system of Equations 12 and adding the three equations, we obtain

$$\frac{\partial^2 q}{\partial x^2} + \frac{\partial^2 q}{\partial y^2} + \frac{\partial^2 q}{\partial z^2} = \left(\frac{\partial f_x}{\partial x} + \frac{\partial f_y}{\partial y} + \frac{\partial f_z}{\partial z}\right) + \left(\frac{\partial g_x}{\partial x} + \frac{\partial g_y}{\partial y} + \frac{\partial g_z}{\partial z}\right) \tag{16}$$

which has the form of a Poisson type equation as:

$$\nabla^2 q = \vec{\nabla}\left(\vec{f} + \vec{g}\right) \tag{17}$$

As $q$ tends to zero at infinity, the Poisson type equation can be solved using Green's function. The solution for the field $q$ is then given by:

$$\begin{aligned} q_{(f,g,x,y,z)} = &\frac{1}{4\pi}\iiint \frac{f_x\left(x-\eta\right) + f_y\left(y-\zeta\right) + f_z\left(z-\chi\right)}{\left(\left(x-\eta\right)^2 + \left(y-\zeta\right)^2 + \left(z-\chi\right)^2\right)^{\frac{3}{2}}} d\eta d\zeta d\chi + \\ &\frac{1}{4\pi}\iiint \frac{g_x\left(x-\eta\right) + g_y\left(y-\zeta\right) + g_z\left(z-\chi\right)}{\left(\left(x-\eta\right)^2 + \left(y-\zeta\right)^2 + \left(z-\chi\right)^2\right)^{\frac{3}{2}}} d\eta d\zeta d\chi \end{aligned} \tag{18}$$

where the integration coordinate system $\eta$, $\zeta$ and $\chi$ overlaps with the $x$, $y$, $z$ coordinate system, and $\vec{f}$ and $\vec{g}$ are set as functions of $\eta$, $\zeta$ and $\chi$.

To simplify the writing of the equations, the force fields are defined as $\vec{k} = \vec{f} + \vec{g}$. Rewriting Equation 18 as

$$q_{(k,x,y,z)} = \frac{1}{4\pi}\iiint \frac{k_x\left(x-\eta\right) + k_y\left(y-\zeta\right) + k_z\left(z-\chi\right)}{\left(\left(x-\eta\right)^2 + \left(y-\zeta\right)^2 + \left(z-\chi\right)^2\right)^{\frac{3}{2}}} d\eta d\zeta d\chi \tag{19}$$

Next, the system of Equations 12 and Equation 19 are combined. First, assume the existence of a function $\Phi$ and set of perturbation terms $u'_{x,y,z}$ such that the velocity perturbation are defined as

$$\begin{aligned} u_x &= u'_x + \frac{\partial \Phi}{\partial x} \\ u_y &= u'_y + \frac{\partial \Phi}{\partial y} \\ u_z &= u'_z + \frac{\partial \Phi}{\partial z} \end{aligned} \tag{20}$$

where $u'_{x,y,z}$ is determined from the equations below:

$$\begin{aligned} \frac{\partial u'_x}{\partial x} &= \frac{k_x}{U_\infty^2 \rho} \\ \frac{\partial u'_y}{\partial x} &= \frac{k_y}{U_\infty^2 \rho} \\ \frac{\partial u'_z}{\partial x} &= \frac{k_z}{U_\infty^2 \rho} \end{aligned} \tag{21}$$

The sets of Equations 20 and 21 in combination with the system of Equations 12 imply Equation 22.

$$\frac{\partial \Phi}{\partial x} = -\frac{q}{\rho U_\infty^2} \tag{22}$$

These equations can now be solved by integrating along $x$. The boundary condition at infinitely upstream ($x = -\infty$) of the force field imposes a non-perturbed flow $[u_x; u_y; u_x]_{x=-\infty} = [0; 0; 0]$.

The $u'_{x,y,z}$ terms can then be obtained from an integration along a line parallel to $x$, where $\eta$ is the integration variable:

$$\begin{aligned} u'_x &= \frac{1}{U_\infty^2 \rho} \int_{-\infty}^{x} k_x d\eta \\ u'_y &= \frac{1}{U_\infty^2 \rho} \int_{-\infty}^{x} k_y d\eta \\ u'_z &= \frac{1}{U_\infty^2 \rho} \int_{-\infty}^{x} k_z d\eta \end{aligned} \tag{23}$$

Equation 22 shows that the solution of $\Phi_{(x,y,z)}$ requires the integration of Equation 19 from $x = -\infty$ to $x$. Setting an integration variable $\xi$ parallel to $x$ and $\eta$ and $q = 0$ at $x = -\infty$ , implies $\Phi_{x=-\infty} = constant$. The integral is written as:

$$\Phi_{(k,x,y,z)} = \int_{-\infty}^{x} \left( -\frac{1}{4\pi \rho U_\infty^2} \iiint \frac{k_x (x-\eta) + k_y (y-\zeta) + k_z (z-\chi)}{\left( (x-\eta)^2 + (y-\zeta)^2 + (z-\chi)^2 \right)^{\frac{3}{2}}} d\eta d\zeta d\chi \right) d\xi \tag{24}$$

Integrating first along $\xi$ results in

$$\Phi_{(k,x,y,z)} = \frac{1}{4\pi\rho U_\infty^2} \iiint \frac{k_x}{r} - \frac{k_y\left(y-\zeta\right)+k_z\left(z-\chi\right)}{r\left(r-\left(x-\eta\right)\right)} d\eta d\zeta d\chi \tag{25}$$

where $r = \sqrt{\left(x-\eta\right)^2+\left(y-\zeta\right)^2+\left(z-\chi\right)^2}$. $u_{x,y,z}$ is determined by inputting Equations 25 and 23 in 20. The results are

$$u_x = \frac{1}{4\pi U_\infty^2\rho} \iiint -\frac{k_x\left(x-\eta\right)+k_y\left(y-\zeta\right)+k_z\left(z-\chi\right)}{r^3} d\eta d\zeta d\chi + \frac{1}{U_\infty^2\rho}\int_{-\infty}^{x} k_x d\eta \tag{26}$$

$$\begin{aligned} u_y =& \frac{1}{4\pi\rho U_\infty^2} \iiint -k_x\frac{\left(y-\zeta\right)}{r^3} d\eta d\zeta d\chi + \\ & \frac{1}{4\pi\rho U_\infty^2} \iiint k_y\frac{\left(r^2-\left(y-\zeta\right)^2\right)\left(r-\left(x-\eta\right)\right)+\left(y-\zeta\right)^2 r}{r^3\left(r-\left(x-\eta\right)\right)^2} d\eta d\zeta d\chi + \\ & \frac{1}{4\pi\rho U_\infty^2} \iiint k_z\frac{\left(z-\chi\right)\left(y-\zeta\right)\left(2r-\left(x-\eta\right)\right)}{r^3\left(r-\left(x-\eta\right)\right)^2} d\eta d\zeta d\chi + \\ & \frac{1}{U_\infty^2\rho}\int_{-\infty}^{x} k_y d\eta \end{aligned} \tag{27}$$

$$\begin{aligned} u_z =& \frac{1}{4\pi\rho U_\infty^2} \iiint -k_x\frac{\left(z-\chi\right)}{r^3} d\eta d\zeta d\chi + \\ & \frac{1}{4\pi\rho U_\infty^2} \iiint k_z\frac{\left(r^2-\left(z-\chi\right)^2\right)\left(r-\left(x-\eta\right)\right)+\left(z-\chi\right)^2 r}{r^3\left(r-\left(x-\eta\right)\right)^2} d\eta d\zeta d\chi + \\ & \frac{1}{4\pi\rho U_\infty^2} \iiint k_y\frac{\left(y-\zeta\right)\left(z-\chi\right)\left(2r-\left(x-\eta\right)\right)}{r^3\left(r-\left(x-\eta\right)\right)^2} d\eta d\zeta d\chi + \\ & \frac{1}{U_\infty^2\rho}\int_{-\infty}^{x} k_z d\eta \end{aligned} \tag{28}$$

## 2.2 Equations for the 2D Actuator Cylinder.

In 2D flow (see (Madsen, 1983)), Equation 24 becomes:

$$\Phi_{(k,x,y)} = \int_{-\infty}^{x}\left(-\frac{1}{2\pi\rho U_\infty^2}\iint \frac{k_x\left(x-\eta\right)+k_y\left(y-\zeta\right)}{\left(x-\eta\right)^2+\left(y-\zeta\right)^2} d\eta d\zeta\right) d\xi \tag{29}$$

The 2D form of the velocity equations are

$$u_x = \frac{1}{2\pi\rho U_\infty^2}\iint -\frac{k_x\left(x-\eta\right)+k_y\left(y-\zeta\right)}{r^2} d\eta d\zeta + \frac{1}{U_\infty^2\rho}\int_{-\infty}^{x} k_x d\eta \tag{30}$$

$$u_y = \frac{1}{2\pi\rho U_\infty^2}\iint -\frac{-k_y\left(x-\eta\right)+k_x\left(y-\zeta\right)}{r^2} d\eta d\zeta + \frac{1}{U_\infty^2\rho}\int_{-\infty}^{x} k_y d\eta \tag{31}$$

## 2.3 Linearised equations and engineering correction

Because the "induction forces" $g_{x,y,z}$ are dependent on the velocity field, Equations 26, 27, 28, 30 and 31 are a nonlinear system which requires an iterative process to solve (see e.g. (Madsen, 1983)). For several flow fields the contribution of the "induction forces" is small and the system can be linearised by assuming $\vec{g} = 0$, $\vec{k} = \vec{f}$. The solution will be the same as a linear vortex model, meaning a vortex model where the free vorticity convects with $U_\infty$. However, a wind turbine or propeller are cases where $g_{x,y,z}$ are significant, especially for high thrust forces. The approach in this work uses the linearised equations ($\vec{k} = \vec{f}$) and modifies the linear solution with an engineering correction. This is justified by a good correlation of the results from a full non-linear 2D Actuator Cylinder model and a modified linear model where the induced velocities are scaled with one single correction factor which is a function of the load or induction level ((Madsen, Larsen, Schmidt Paulsen, & Vita, 2013)). This approach is also used in vortex models, either correcting the wake density (implying a correction in the force field) or directly correcting the velocity field.

The engineering correction scales the induction field $u_{x,y,z}$ by a single factor which satisfies the continuity equation. The correction is based on the application to an actuator with the thrust aligned with $U_\infty$. A more accurate correction might consider a linear decomposition of the induction due to forces aligned and perpendicular to $U_\infty$. To derive the correction, consider a planar actuator perpendicular to $U_\infty$ (surface in the $yz$-plane), with a force field $\vec{f} = [f_x; 0; 0]$. The actuator disc momentum theory (Glauert, 1948) states that at the actuator:

$$\frac{f_x}{\frac{1}{2}\rho U_\infty^2} = 4u_{x_{mt}}\left(1 + u_{x_{mt}}\right) \tag{32}$$

where the subscript $mt$ stands for momentum theory. Equation 32 is written in the form commonly applied in propeller theory.

However, Equations 26 and 30 give

$$\frac{f_x}{\frac{1}{2}\rho U_\infty^2} = 4u_x \tag{33}$$

Combining Equations 32 and 33 yields an expression for the correction factor $c_{orr}$ as

$$c_{orr} = \frac{u_{x_{mt}}}{u_x} = \frac{1}{1 + u_{x_{mt}}} \tag{34}$$

Considering the entire actuator with a total thrust in $x$-direction $F_x$, the thrust coefficient $C_T$ is defined as

$$C_T = \frac{F_x}{\frac{1}{2}\rho U_\infty^2} = 4u_{x_{mt}}\left(1 + u_{x_{mt}}\right) \tag{35}$$

and

$$c_{orr} = \frac{1}{1 + \frac{1}{2}\left(\sqrt{1 - C_T} - 1\right)} \tag{36}$$

The solutions presented are corrected by this factor, when required. Additionally, the reference induction factor $a_0$ is defined as

$$a_0 = -\frac{u_{x_{mt}}}{U_\infty} = -\frac{1}{2}\left(\sqrt{1 - C_T} - 1\right) \tag{37}$$

## 2.4 Blade element model and tip correction

The inflow angle is provided by the AC model. This dynamic inflow angle is fed into the blade element model as an input. The blade element model is built on previously calculated airfoil polars, with a dynamic stall model added for unsteady effects. The blade element calculates the lift, drag and moment at the airfoil section. To account for tip effects, a tip correction model is used. The tip correction model is based on a modified Prandtl's tip correction model.

# 3 Deliverable Outcome: structural model and one-way coupling aeroelastic model

A finite element model is able to simulate a variety of loading and operational dynamics of interest. However, to capture long-term temporal dynamic events, the full structural model's computational time is prohibitively expensive. A Multi-Body Dynamics (MBD) simulation is an efficient and sufficiently accurate way to simulate long duration loading events.

The MBD model and the aeroelastic tool need to be validated as able to model a VAWT. The chosen case was the TU Delft's experimental H-VAWT: *PitchVAWT* [Figure 2 and Figure 3 from (B. LeBlanc & Simao Ferreira, 2018)]. The choice of this case is based on:

- The *PitchVAWT* will be used in the development of deliverable *D2.2* of this project and much of the respective experimental research.
- The aeroelastic behaviour (aerodynamics and structural dynamics) of the *PitchVAWT* has been experimentally and numerically studied and the tools have been validated [see (LeBlanc & Ferreira, n.d.),(LeBlanc & Ferreira, 2020),(Leblanc & Ferreira, 2020),(B. P. LeBlanc & Ferreira, 2018)].
- A finite element model of the *PitchVAWT* has been developed, which can be used as a high fidelity validation of the MBD model (see Figure 4 from (LeBlanc & Ferreira, 2020)).

## 3.1 Multibody Dynamics Simulation

The Multibody Dynamics Simulation is implemented in the Siemens Simcenter Motion environment, which can incorporate rigid motion bodies to understand general loading dynamics or flexible motion for bodies with internal stresses or displacements, such as blade motion and deformation. A modal space representation of the component is used to model the flexible dynamics.

The structural model was divided into three distinct components. The first body is the rotor, which is made up of the blades, struts, tower, and non-structural masses that represent the connection components. The second is the turbine base, which is made up of a steel beam support structure and houses the main bearing housing and drive-line. The third component is the mounting platform. Each motion body is labeled in Figure 5.

Joints connect all three components. Two bearings connect the rotor to the base, which prevents translation while allowing rotation. The lower bearing is a revolute joint that controls the rotational speed. In all six degrees of freedom, the base is rigidly attached to the platform.

The included modes for each flexible body determine the available combinations that can be processed in the response. As a result, it is critical to include as many modes as necessary to properly capture the dynamics.

## 3.2 One-way coupling or aerodynamic loads for simulation of experimental case.

For the small scale experimental VAWT, the structural inertial loads are larger than the aerodynamic loads. Therefore, a one way coupling of the aerodynamic loads has proven sufficient for an accurate aeroelastic simulation.

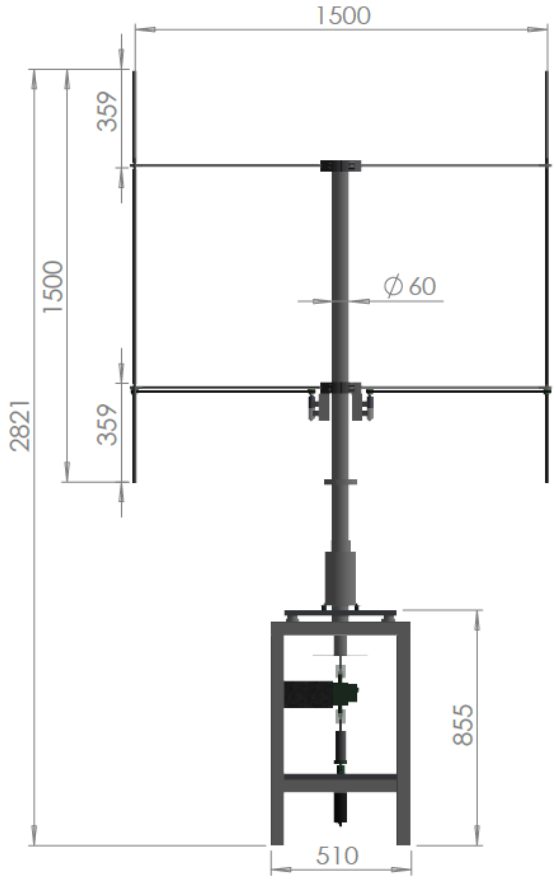


*Figure 2: PitchVAWT model, dimensions in mm.*

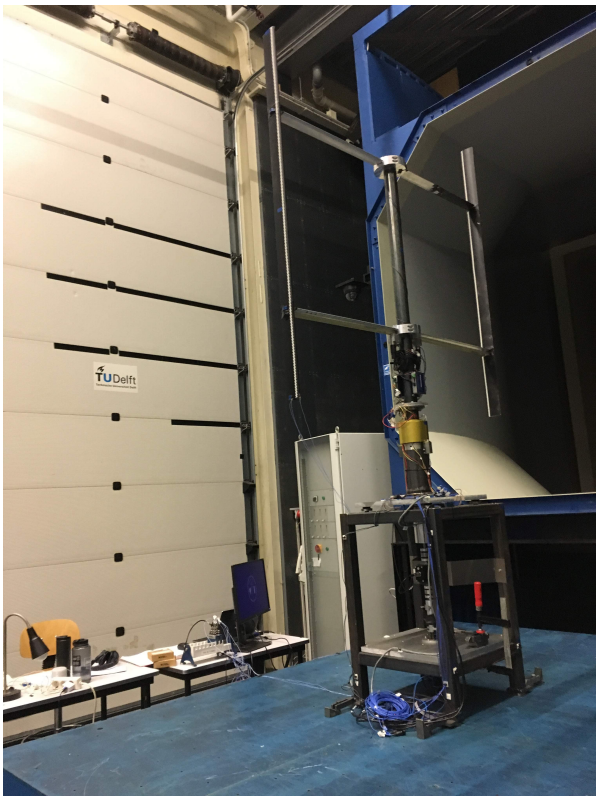


*Figure 3: PitchVAWT installed in TU Delft's Open Jet Facility.*

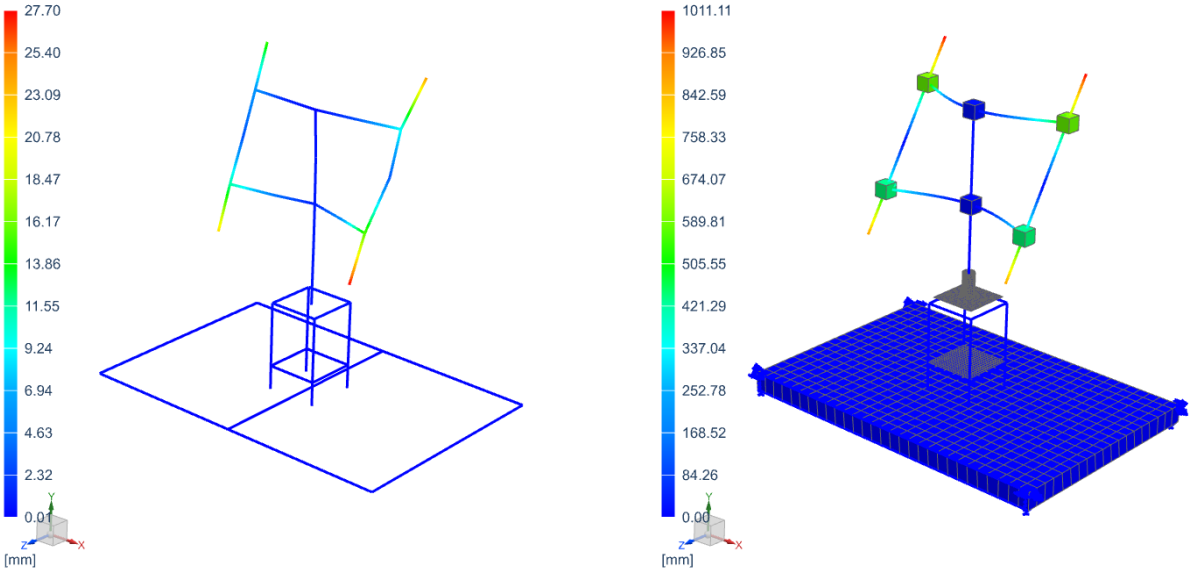


*Figure 4: Comparison of VAWT mode between experimental modal data (left) and finite element simulation (right).*

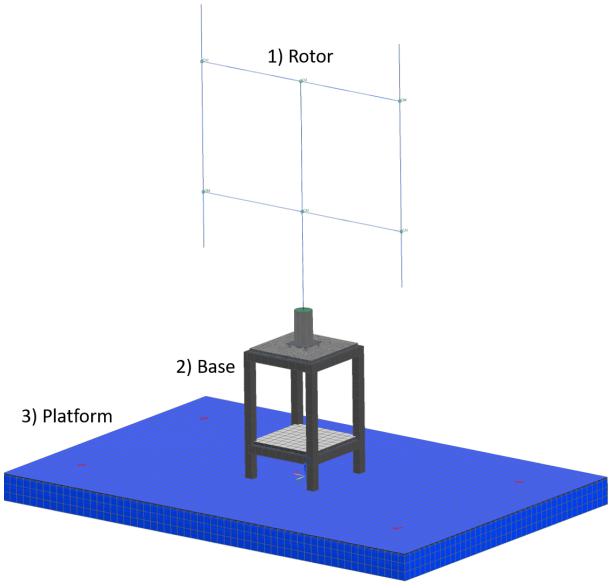


*Figure 5: Flexible VAWT model with motion bodies identified. 1) Main rotor, 2) Base structure, 3) Grounding platform*

For a tip speed ratio (TSR) of 4, the normal and tangential aerodynamic loads are first calculated using the Actuator Cylinder model introduced in Section 2. Within Simcenter Motion's MBD model, vector loads are applied to the appropriate blade in the corresponding normal and tangential directions.

The turbine's response at TSR= 4 was calculated using both flexible and rigid bodies. The rotor is displaced and deformed asymmetrically as a result of the aerodynamic loading. In the structure, the thrust force oscillates around a mean that is offset from zero in the x-direction (against the wind), whereas the thrust perpendicular to the wind direction oscillates around zero. The torque oscillates with the 2P response frequency and has a sign consistent with the need to prevent the rotor from speeding up. These results are in accordance with the applied loading.

The comparison of flexible and rigid body simulations reveals that the inertial dynamics of the flexible bodies, particularly the platform, have a significant impact on the rotor base's experienced loads. Because of the side-to-side motion of the platform and the inertial loading of the turbine in response, the experienced loads of the turbine at the base are greater. This confirms the need to ensure that the natural frequencies of oscillation of the support structure do not interact unfavorably with the rotor dynamics and that support structure stiffness is properly considered in the design (see also (Amiri & Carroll, 2021)).

The results of these simulations are in process of publication and are not included in this report, with the exception of Figure 6, to demonstrate the inclusion of gravity in the simulation and its impact on rotor deformation.

The multibody dynamics model is capable of accurately capturing most dynamics of interest and can be used to predict turbine response due to dynamic pitching of the VAWT. Individual component test results were positive and in good agreement with experimental data and the higher fidelity model. The dynamics of the support structure have a significant impact on the turbine response at specific frequencies of interest. The model is capable of capturing the platform dynamics and their impact on the turbine's response. The one-way coupling of the

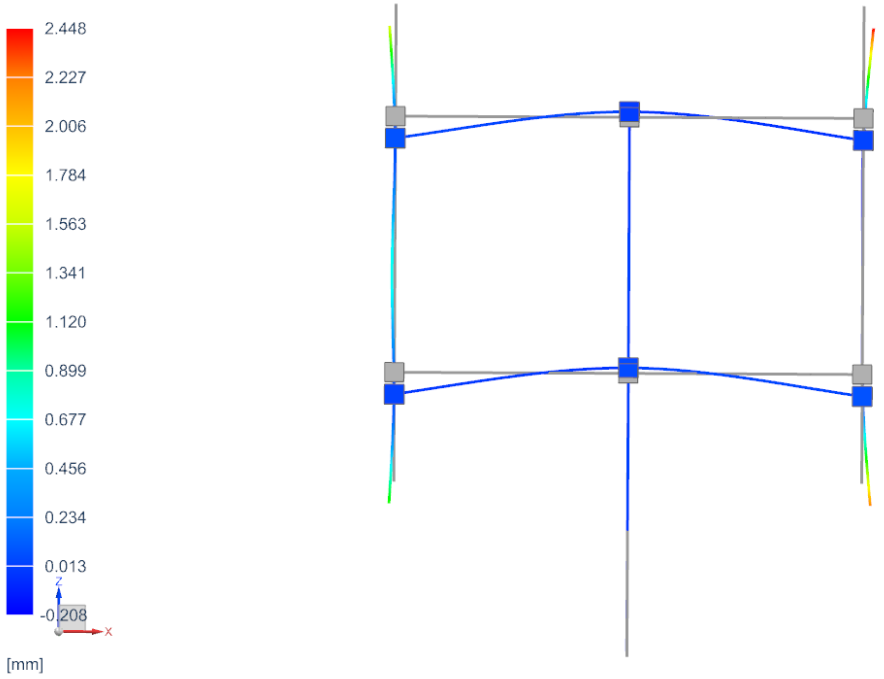


*Figure 6: Rotor deformation including gravity and blade loading at tip speed ratio 4, coloring shows radial deformation.*

aerodynamic model was successful.

# 4 Deliverable Outcome: results of the aerodynamic simulations of the X-Rotor's primary rotor

## 4.1 Description of the primary rotor of the X-Rotor concept

The description of the primary rotor of the X-Rotor concept was originally provided in (Leithead, Camciuc, Amiri, & Carroll, 2019) and (Amiri & Carroll, 2021). The X-Rotor design comprises a primary vertical axis rotor that consists of an upper and lower section with relatively typical blades that are angled both upwards and downwards from the ends of a relatively short, stiff cross-arm. In this report we will consider the two blade X-Rotor as shown in Figure 7 (from (Amiri & Carroll, 2021)) . The upper section's primary function is to contribute significantly to the extraction of mechanical energy from the wind.

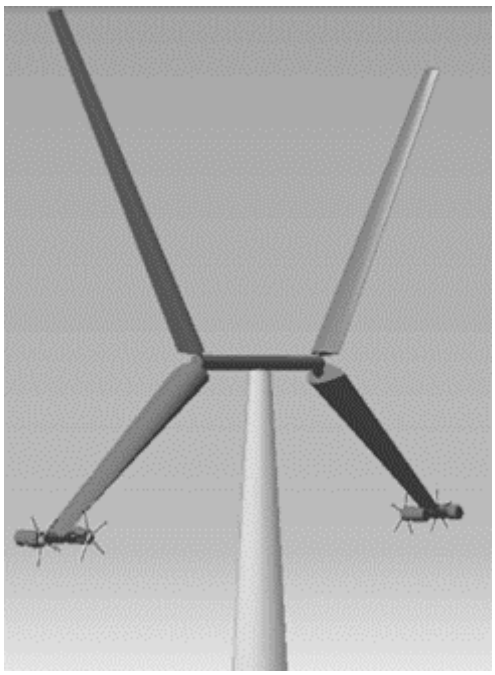

*Figure 7: X-Rotor with two blades.*

Table 1 presents the primary scales of the rotor and operational conditions.

In this analysis, the X-Rotor is simplified into the *Upper/Top Blade* and *Lower/Bottom Blade*, as presented in Figure 8 (from (Amiri & Carroll, 2021)). The blades are assumed to be contiguous. Table 2 and Table 3 present the control sections that define the geometry of the blades.

## 4.2 Rotor performance: power and thrust with collective pitch control

The simulations were conducted for a wind speed interval $[4m/s..19.5m/s]$. Only the **Upper/Top Blades** are allowed to pitch. The pitch is collective and constant over the rotation, for each wind speed. The control target is constant power above rated wind speed $12.5m/s$. The detailed results of the simulations are stored in the database files (folder "SimulationsOperationalCurve"), with individual files for each wind speed.

*Table 1: Primary rotor parameters.*

| | Upper Rotor | Lower Rotor | |
|---|---|---|---|
| Height | 86,6 | 42,1 | $m$ |
| Radius bottom | 25 | 25 | $m$ |
| Radius top | 75 | 75 | $m$ |
| Area | 8660 | 4210 | $m^2$ |
| # blades | 2 | 2 | |
| Blade length | 100 | 65,3 | $m$ |
| Design tip speed ratio $\lambda$ | 5 | 5 | |
| Tip speed | 62,5 | 62,5 | $m/s$ |

| Rotor | | |
|---|---|---|
| $U_\infty$ | 12,5 | $m/s$ |
| $\rho$ | 1,255 | $kg/m^3$ |
| Rotational speed | 0,83 | $rad/s$ |
| Total rotor aerodynamic area | 12870 | $m^2$ |

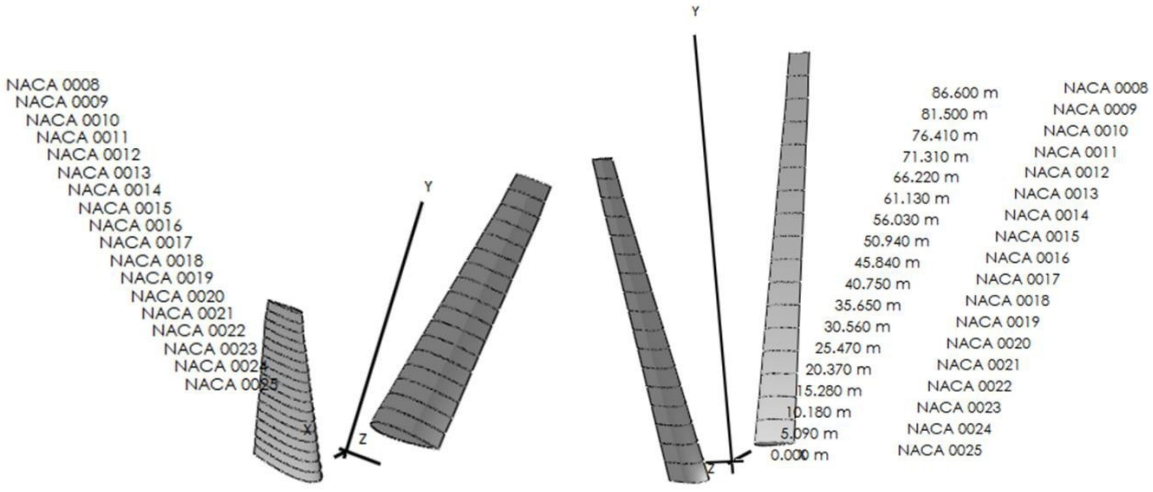


*(a) Lower blade* *(b) Upper blade*

*Figure 8: Representations of the blades with their airfoils.*

*Table 2: Parametric definition of the original upper/top blade.*

| Section | Height | Chord | Radius | Twist | Pitching axis | Foil | Reynolds # |
|---|---|---|---|---|---|---|---|
| 1 | 0.00 | 10.00 | 25.00 | 0.00 | 0.25 | NACA 0025 | $1.4*10^7$ |
| 2 | 5.09 | 9.71 | 27.94 | 0.00 | 0.26 | NACA 0024 | $1.5*10^7$ |
| 3 | 10.19 | 9.41 | 30.88 | 0.00 | 0.26 | NACA 0023 | $1.6*10^7$ |
| 4 | 15.28 | 9.12 | 33.82 | 0.00 | 0.27 | NACA 0022 | $1.7*10^7$ |
| 5 | 20.38 | 8.82 | 36.76 | 0.00 | 0.28 | NACA 0021 | $1.8*10^7$ |
| 6 | 25.47 | 8.53 | 39.71 | 0.00 | 0.29 | NACA 0020 | $1.9*10^7$ |
| 7 | 30.56 | 8.24 | 42.65 | 0.00 | 0.30 | NACA 0019 | $2.0*10^7$ |
| 8 | 35.66 | 7.94 | 45.59 | 0.00 | 0.31 | NACA 0018 | $2.0*10^7$ |
| 9 | 40.75 | 7.65 | 48.53 | 0.00 | 0.32 | NACA 0017 | $2.1*10^7$ |
| 10 | 45.85 | 7.35 | 51.47 | 0.00 | 0.33 | NACA 0016 | $2.1*10^7$ |
| 11 | 50.94 | 7.06 | 54.41 | 0.00 | 0.34 | NACA 0015 | $2.1*10^7$ |
| 12 | 56.04 | 6.76 | 57.35 | 0.00 | 0.36 | NACA 0014 | $2.2*10^7$ |
| 13 | 61.13 | 6.47 | 60.29 | 0.00 | 0.37 | NACA 0013 | $2.2*10^7$ |
| 14 | 66.22 | 6.18 | 63.24 | 0.00 | 0.39 | NACA 0012 | $2.2*10^7$ |
| 15 | 71.32 | 5.88 | 66.18 | 0.00 | 0.40 | NACA 0011 | $2.2*10^7$ |
| 16 | 76.41 | 5.59 | 69.12 | 0.00 | 0.42 | NACA 0010 | $2.1*10^7$ |
| 17 | 81.51 | 5.29 | 72.06 | 0.00 | 0.47 | NACA 0009 | $2.1*10^7$ |
| 18 | 86.60 | 5.00 | 75.00 | 0.00 | 0.50 | NACA 0008 | $2.1*10^7$ |

*Table 3: Parametric definition of the original lower/bottom blade.*

| Section | Height | Chord | Radius | Twist | Pitching axis | Foil | Reynolds # |
|---|---|---|---|---|---|---|---|
| 1 | 0.00 | 14.00 | 25.00 | 0.00 | 0.25 | NACA 0025 | $1.9*10^7$ |
| 2 | 2.48 | 13.59 | 27.94 | 0.00 | 0.26 | NACA 0024 | $2.1*10^7$ |
| 3 | 4.95 | 13.18 | 30.88 | 0.00 | 0.26 | NACA 0023 | $2.3*10^7$ |
| 4 | 7.43 | 12.76 | 33.82 | 0.00 | 0.27 | NACA 0022 | $2.4*10^7$ |
| 5 | 9.91 | 12.35 | 36.76 | 0.00 | 0.28 | NACA 0021 | $2.5*10^7$ |
| 6 | 12.38 | 11.94 | 39.71 | 0.00 | 0.29 | NACA 0020 | $2.6*10^7$ |
| 7 | 14.86 | 11.53 | 42.65 | 0.00 | 0.30 | NACA 0019 | $2.7*10^7$ |
| 8 | 17.34 | 11.12 | 45.59 | 0.00 | 0.31 | NACA 0018 | $2.8*10^7$ |
| 9 | 19.81 | 10.71 | 48.53 | 0.00 | 0.32 | NACA 0017 | $2.9*10^7$ |
| 10 | 22.29 | 10.29 | 51.47 | 0.00 | 0.33 | NACA 0016 | $2.9*10^7$ |
| 11 | 24.76 | 9.88 | 54.41 | 0.00 | 0.34 | NACA 0015 | $3.0*10^7$ |
| 12 | 27.24 | 9.47 | 57.35 | 0.00 | 0.36 | NACA 0014 | $3.0*10^7$ |
| 13 | 29.72 | 9.06 | 60.29 | 0.00 | 0.37 | NACA 0013 | $3.0*10^7$ |
| 14 | 32.19 | 8.65 | 63.24 | 0.00 | 0.39 | NACA 0012 | $3.0*10^7$ |
| 15 | 34.67 | 8.24 | 66.18 | 0.00 | 0.40 | NACA 0011 | $3.0*10^7$ |
| 16 | 37.15 | 7.82 | 69.12 | 0.00 | 0.42 | NACA 0010 | $3.0*10^7$ |
| 17 | 39.62 | 7.41 | 72.06 | 0.00 | 0.47 | NACA 0009 | $3.0*10^7$ |
| 18 | 42.10 | 7.00 | 75.00 | 0.00 | 0.50 | NACA 0008 | $2.9*10^7$ |

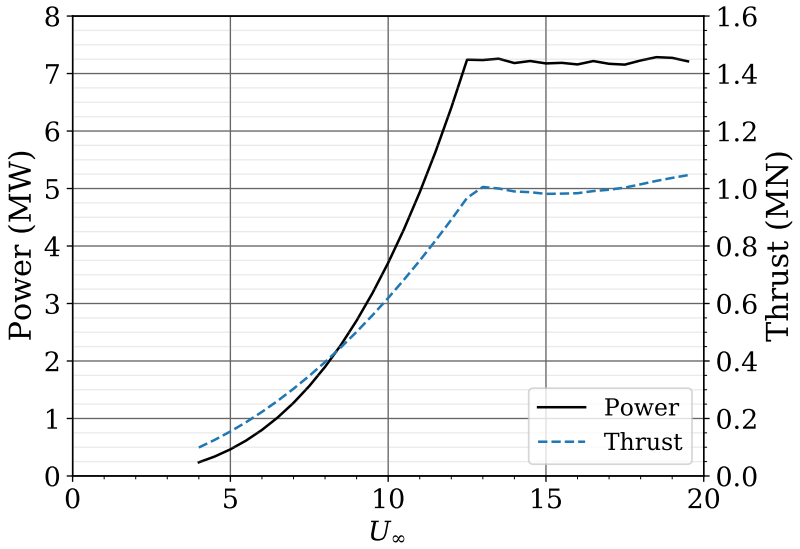


*Figure 9: Aerodynamic Power and Thrust as function of wind speed $U_\infty$, with collective pitch control, accounting for tip losses.*

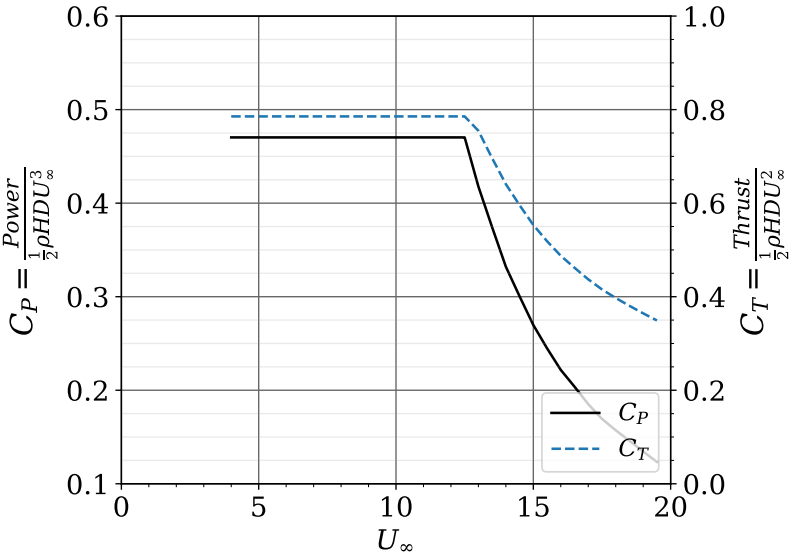


*Figure 10: Aerodynamic Power ($C_P$) and thrust ($C_T$) coefficient as function of wind speed $U_\infty$, with collective pitch control, accounting for tip losses.*

Figure 9, Figure 10 and Figure 11 present the aerodynamic power and thrust as function of wind speed $U_\infty$; the equivalent aerodynamic power ($C_P$) and thrust ($C_T$) coefficients; and rotor speed (RPM) and collective blade pitch setting (Top Blade). These results are detailed in Table 4.

The rated aerodynamic power is $7.241MW$ at rated wind speed $12.5m/s$, at blade pitch of $4°$ and a thrust of $.967MN$. The aerodynamic power coefficient is $C_P = 0.470$ and the aerodynamic thrust coefficient is $C_T = 0.785$. The TSR is $5.0$. The aerodynamic power is higher than reported by (Amiri & Carroll, 2021).

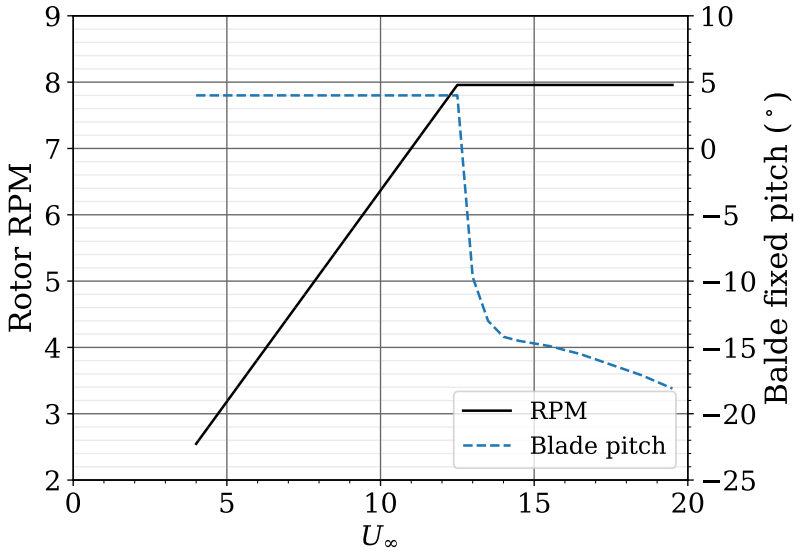


*Figure 11: Rotor speed (RPM) and collective blade pitch setting (Top Blade) as function of wind speed $U_\infty$, with collective pitch control, accounting for tip losses.*

*Table 4: Operational and performance parameters of the X-Rotor primary rotor.*

| $U\infty$ $(m/s)$ | TSR | RPM | Blade pitch ° | $C_P$ | $C_T$ | Power $(MW)$ | Thrust $(MN)$ |
|---|---|---|---|---|---|---|---|
| 4.0 | 5.00 | 2.55 | 4.0 | 0.470 | 0.785 | 0.237 | 0.099 |
| 4.5 | 5.00 | 2.86 | 4.0 | 0.470 | 0.785 | 0.338 | 0.125 |
| 5.0 | 5.00 | 3.18 | 4.0 | 0.470 | 0.785 | 0.463 | 0.155 |
| 5.5 | 5.00 | 3.50 | 4.0 | 0.470 | 0.785 | 0.617 | 0.187 |
| 6.0 | 5.00 | 3.82 | 4.0 | 0.470 | 0.785 | 0.801 | 0.223 |
| 6.5 | 5.00 | 4.14 | 4.0 | 0.470 | 0.785 | 1.018 | 0.262 |
| 7.0 | 5.00 | 4.46 | 4.0 | 0.470 | 0.785 | 1.272 | 0.303 |
| 7.5 | 5.00 | 4.77 | 4.0 | 0.470 | 0.785 | 1.564 | 0.348 |
| 8.0 | 5.00 | 5.09 | 4.0 | 0.470 | 0.785 | 1.898 | 0.396 |
| 8.5 | 5.00 | 5.41 | 4.0 | 0.470 | 0.785 | 2.277 | 0.447 |
| 9.0 | 5.00 | 5.73 | 4.0 | 0.470 | 0.785 | 2.703 | 0.502 |
| 9.5 | 5.00 | 6.05 | 4.0 | 0.470 | 0.785 | 3.178 | 0.559 |
| 10.0 | 5.00 | 6.37 | 4.0 | 0.470 | 0.785 | 3.707 | 0.619 |
| 10.5 | 5.00 | 6.68 | 4.0 | 0.470 | 0.785 | 4.292 | 0.683 |
| 11.0 | 5.00 | 7.00 | 4.0 | 0.470 | 0.785 | 4.934 | 0.749 |
| 11.5 | 5.00 | 7.32 | 4.0 | 0.470 | 0.785 | 5.638 | 0.819 |
| 12.0 | 5.00 | 7.64 | 4.0 | 0.470 | 0.785 | 6.406 | 0.892 |
| 12.5 | 5.00 | 7.96 | 4.0 | 0.470 | 0.785 | 7.241 | 0.967 |
| 13.0 | 4.81 | 7.96 | -9.7 | 0.418 | 0.755 | 7.235 | 1.005 |
| 13.5 | 4.63 | 7.96 | -13.0 | 0.374 | 0.696 | 7.258 | 1.000 |
| 14.0 | 4.46 | 7.96 | -14.2 | 0.332 | 0.641 | 7.182 | 0.990 |
| 14.5 | 4.31 | 7.96 | -14.5 | 0.300 | 0.596 | 7.218 | 0.987 |
| 15.0 | 4.17 | 7.96 | -14.7 | 0.270 | 0.553 | 7.176 | 0.981 |
| 15.5 | 4.03 | 7.96 | -14.9 | 0.245 | 0.519 | 7.186 | 0.982 |
| 16.0 | 3.91 | 7.96 | -15.2 | 0.222 | 0.487 | 7.158 | 0.984 |
| 16.5 | 3.79 | 7.96 | -15.5 | 0.204 | 0.462 | 7.217 | 0.991 |
| 17.0 | 3.68 | 7.96 | -15.9 | 0.185 | 0.437 | 7.169 | 0.996 |
| 17.5 | 3.57 | 7.96 | -16.3 | 0.169 | 0.416 | 7.155 | 1.003 |
| 18.0 | 3.47 | 7.96 | -16.7 | 0.157 | 0.397 | 7.227 | 1.015 |
| 18.5 | 3.38 | 7.96 | -17.1 | 0.146 | 0.380 | 7.285 | 1.027 |
| 19.0 | 3.29 | 7.96 | -17.6 | 0.135 | 0.364 | 7.273 | 1.037 |
| 19.5 | 3.21 | 7.96 | -18.1 | 0.123 | 0.349 | 7.212 | 1.047 |

## 4.3 Loading and inflow properties at rated wind speed $U_\infty = 12.5m/s$

The following sections present inflow and loading results as function of blade span and azimuth position of the primary rotor's upper and lower blades at rated wind speed $U_\infty = 12.5m/s$. Figure 12 shows the inflow angle at blade location in degrees (°). Figure 13 shows the tangential and normal force per meter of span $(N/m)$. Figure 14 shows the flapwise and edgewise bending moment as function of blade span and azimuthal position.

## 4.4 Standstill loading for $U_\infty = 41.0m/s$ and $U_\infty = 52.0m/s$

The rotor blades must be strong enough to withstand extreme loads. The extreme loads correspond to extreme wind speeds of 52m/s with a recurrence period of 50 years, while the turbine is parked, and a simultaneous loss of grid connection may occur (DLC 6.2 of IEC 61400-1, as

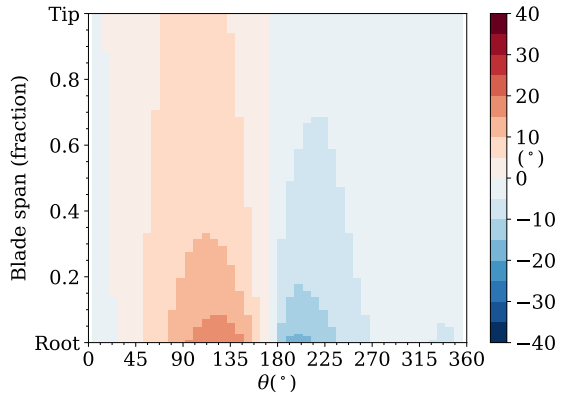


*(a) Lower blade, inflow angle*

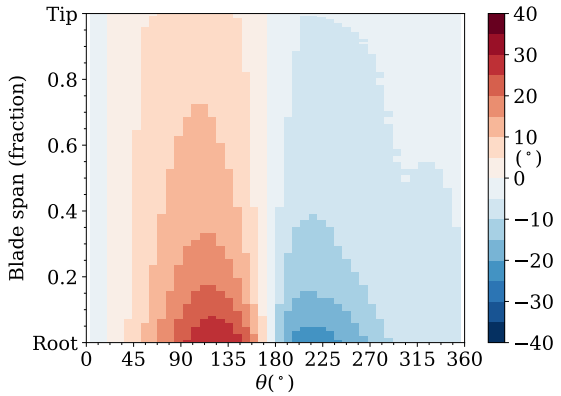


*(b) Upper blade, inflow angle*

*Figure 12: Inflow angle at blade location in degrees (°) as function of blade span and azimuth position $\theta$ of the primary rotor's upper and lower blades at rated wind speed $U_\infty = 12.5 m/s$.*

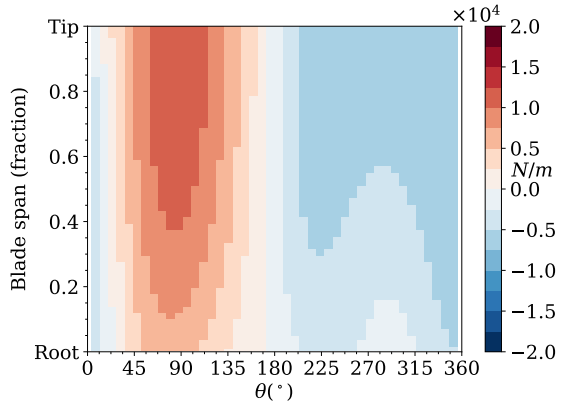


*(a) Lower blade, normal force*

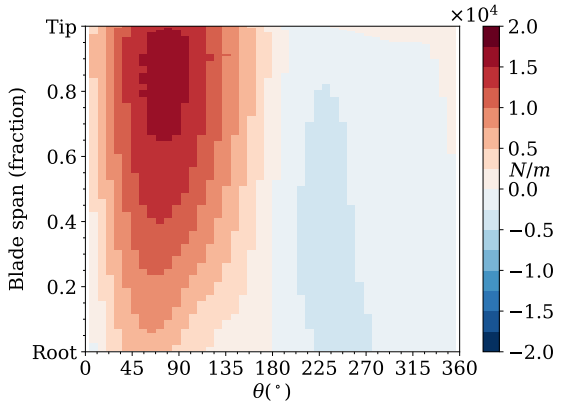


*(b) Upper blade, normal force*

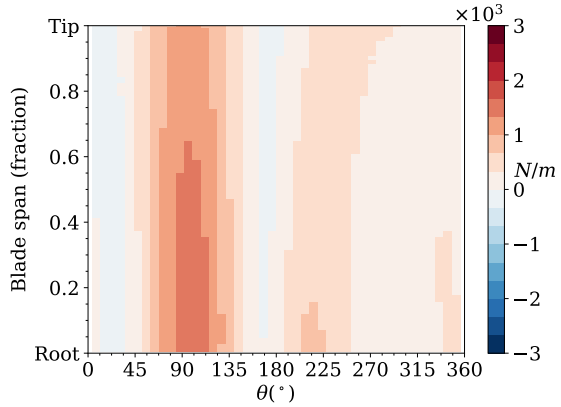


*(c) Lower blade, tangential force*

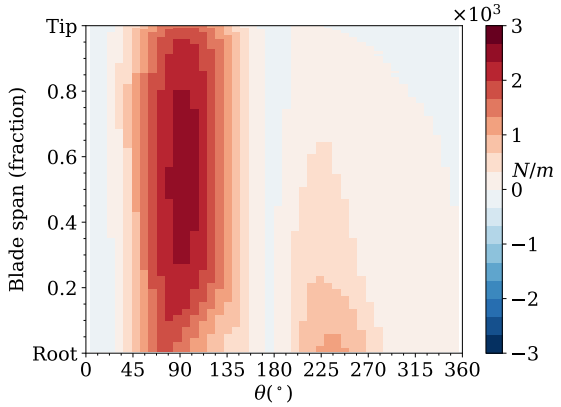


*(d) Upper blade, tangential force*

*Figure 13: Tangential and normal force per meter of span ($N/m$) as function of blade span and azimuth position $\theta$ of the primary rotor's upper and lower blades at rated wind speed $U_\infty = 12.5 m/s$*

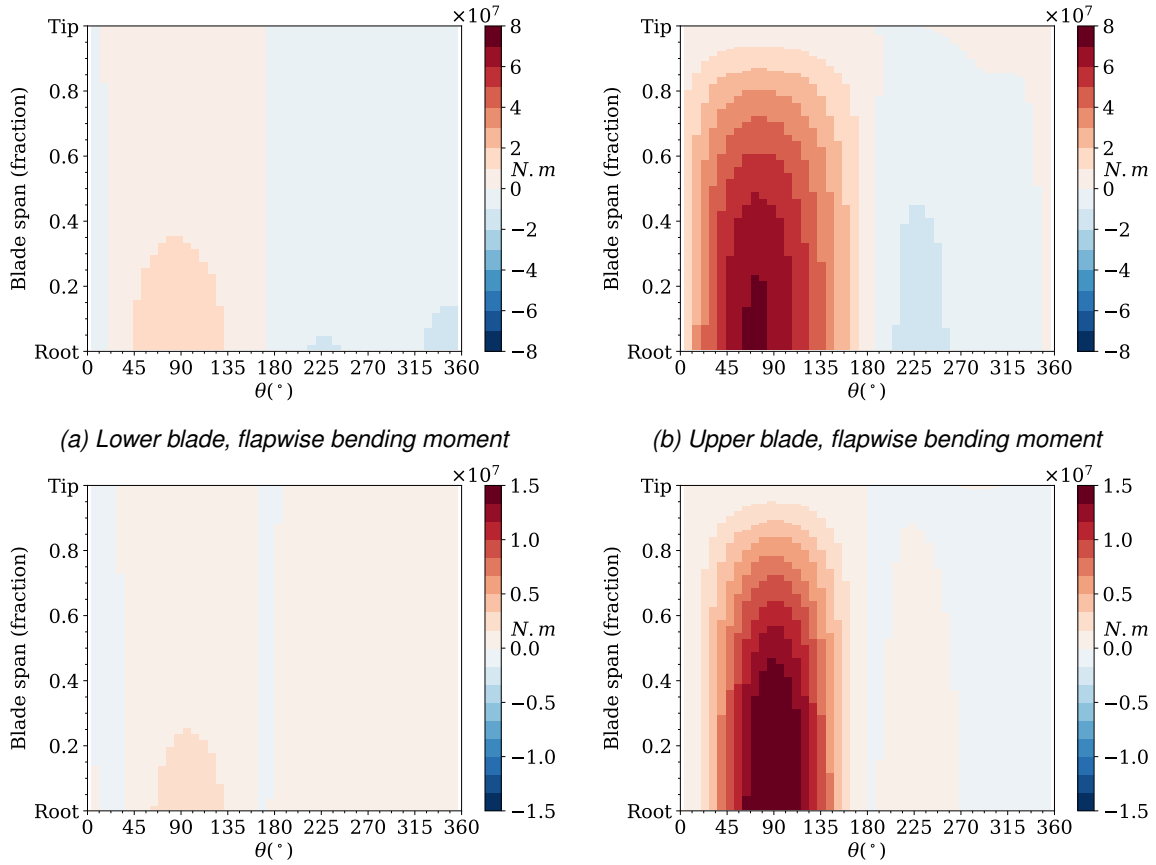


*(a) Lower blade, flapwise bending moment*

*(b) Upper blade, flapwise bending moment*

*(c) Lower blade, edgewise bending moment*

*(d) Upper blade, edgewise bending moment*

*Figure 14: Flapwise and edgewise bending moment as function of blade span and azimuth position $\theta$ of the primary rotor's upper and lower blades at rated wind speed $U_\infty = 12.5m/s$*

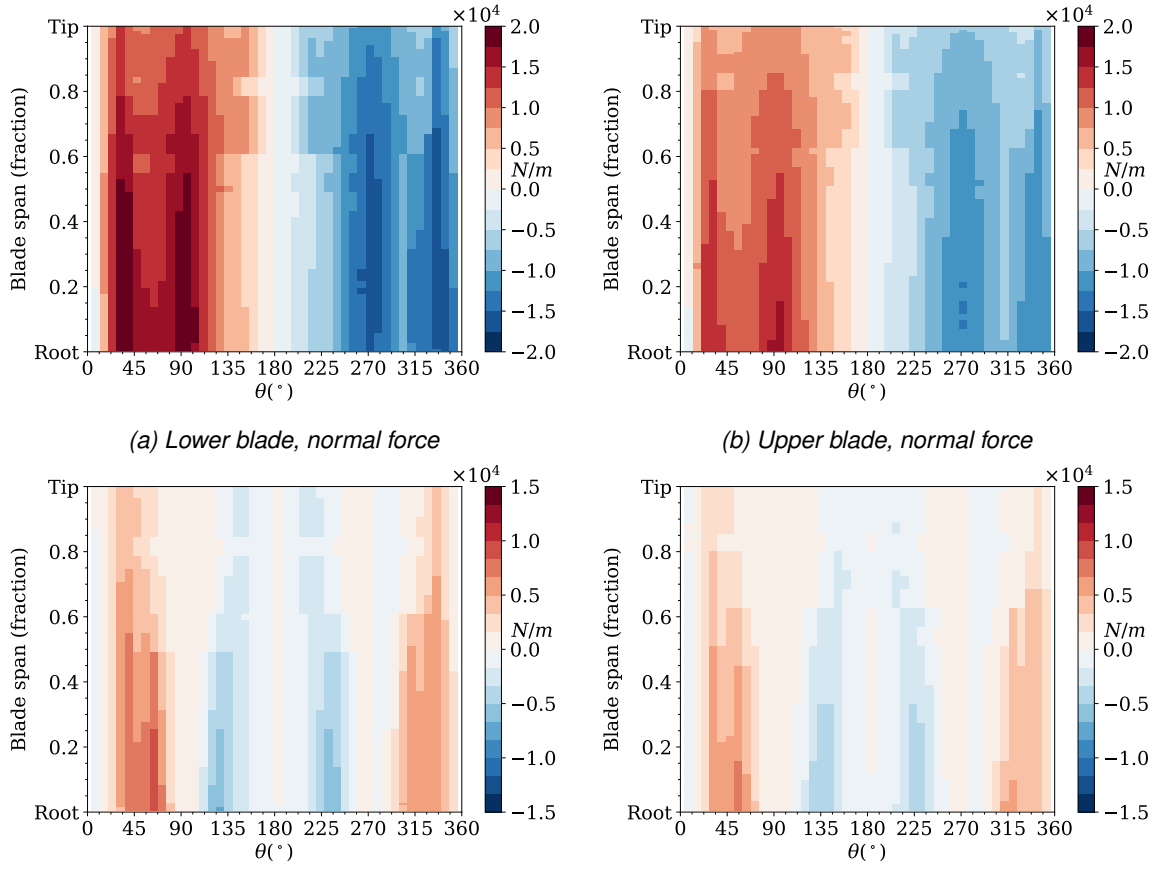


*(a) Lower blade, normal force*

*(b) Upper blade, normal force*

*(c) Lower blade, tangential force*

*(d) Upper blade, tangential force*

*Figure 15: Tangential and normal force per meter of span ($N/m$) as function of blade span and azimuth position $\theta$ of the primary rotor's upper and lower blades for standstill rotor at $U_\infty = 41.0m/s$.*

described by (Amiri & Carroll, 2021)). As a result, the turbine could become locked at any given azimuthal position.

This sections presents loading results as function of blade span and azimuthal position of the primary rotor's upper and lower blades for the case that the rotor is blocked at a stanstill position in a wind speed $U_\infty = 41.0m/s$ and $52.0m/s$. For $U_\infty = 41.0m/s$, Figure 15 shows the tangential and normal force per meter of span ($N/m$); Figure 16 shows the flapwise and edgewise bending moment as function of blade span and azimuth position. For $52.0m/s$, the same results are presented in Figure 17 and Figure 18. The detailed results of the simulations are stored in the database files (folder "SimulationsStandStill"), with individual files for each wind speed and pitch setting.

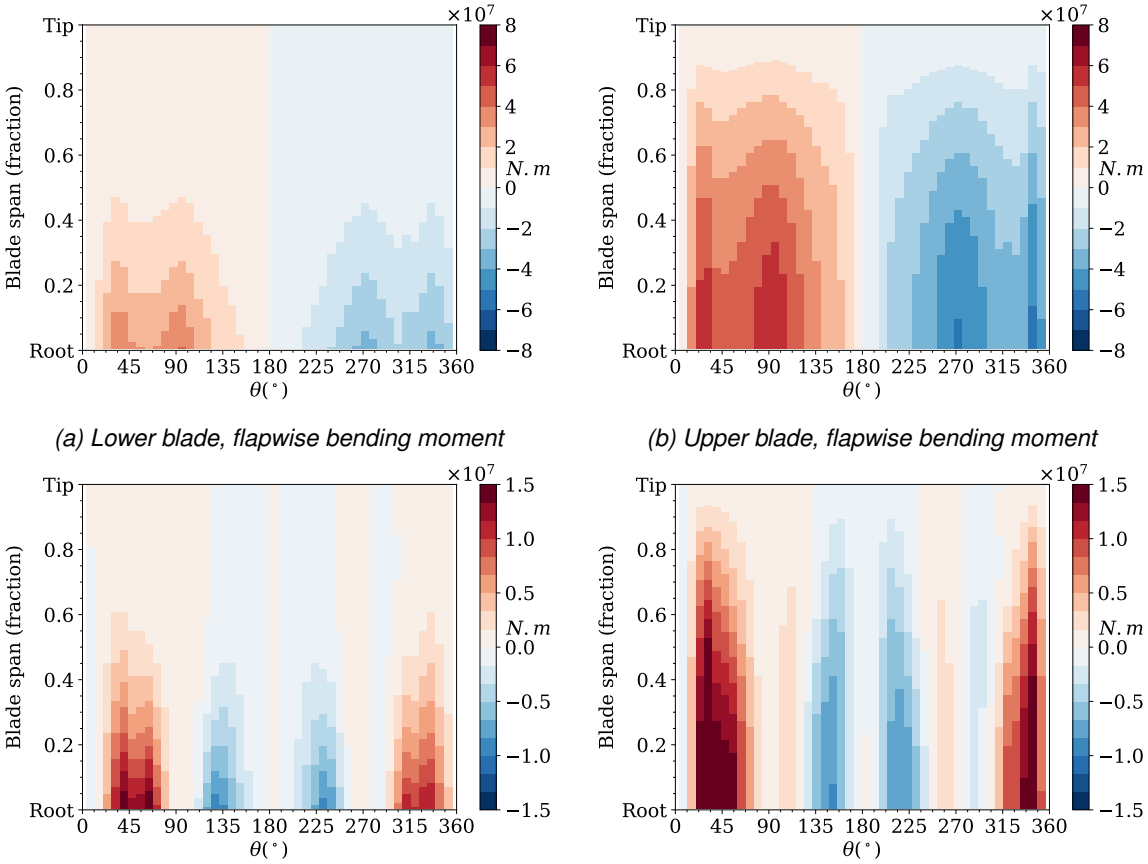


*(a) Lower blade, flapwise bending moment*

*(b) Upper blade, flapwise bending moment*

*(c) Lower blade, edgewise bending moment*

*(d) Upper blade, edgewise bending moment*

*Figure 16: Flapwise and edgewise bending moment as function of blade span and azimuth position $\theta$ of the primary rotor's upper and lower blades for standstill rotor at $U_\infty = 41.0 m/s$.*

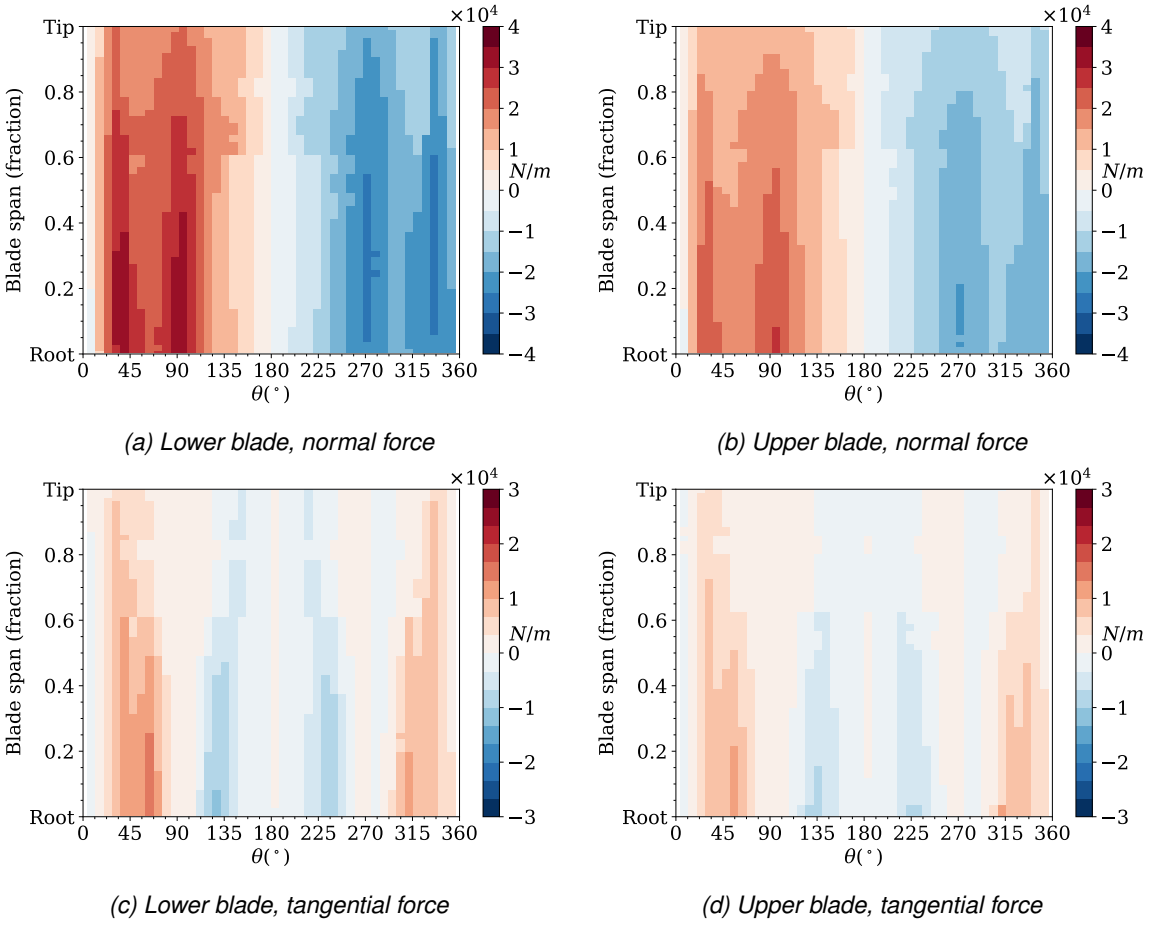


*(a) Lower blade, normal force*

*(b) Upper blade, normal force*

*(c) Lower blade, tangential force*

*(d) Upper blade, tangential force*

*Figure 17: Tangential and normal force per meter of span ($N/m$) as function of blade span and azimuth position $\theta$ of the primary rotor's upper and lower blades for standstill rotor at $U_\infty = 52.0 m/s$.*

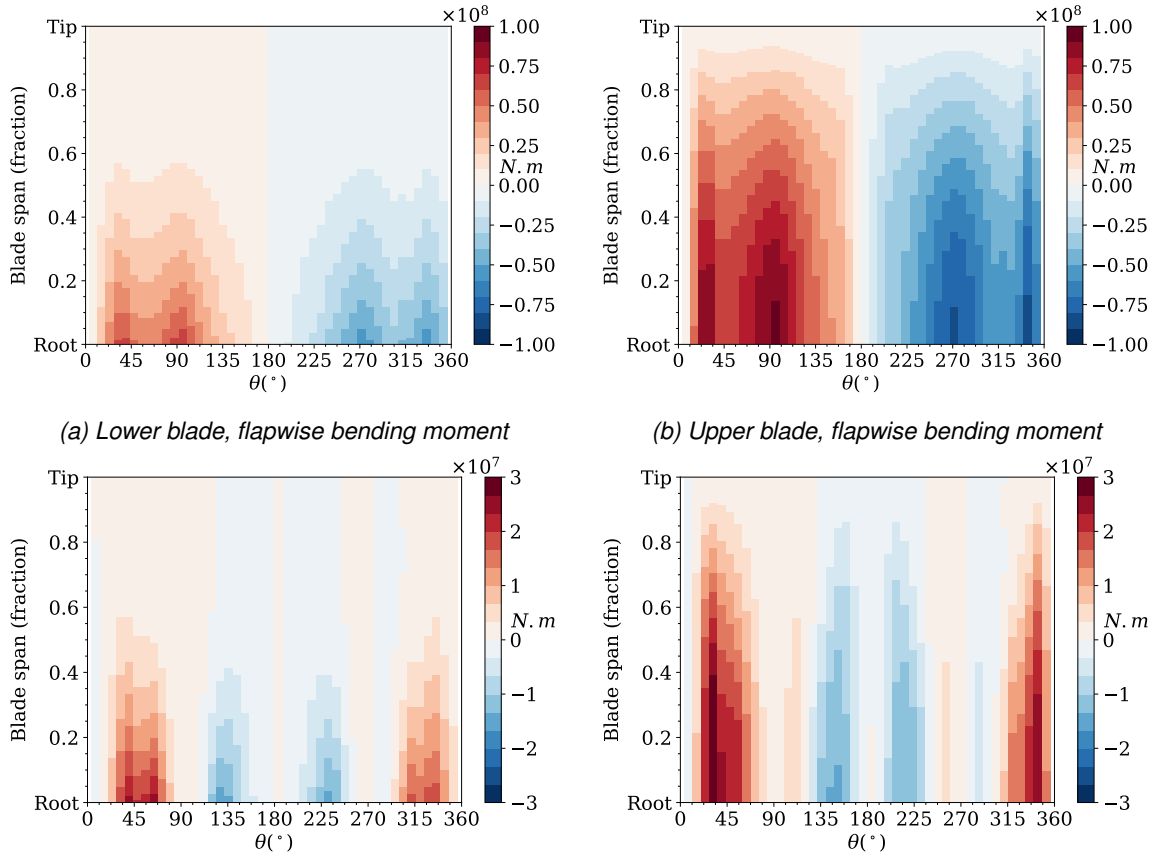


*(a) Lower blade, flapwise bending moment*

*(b) Upper blade, flapwise bending moment*

*(c) Lower blade, edgewise bending moment*

*(d) Upper blade, edgewise bending moment*

*Figure 18: Flapwise and edgewise bending moment as function of blade span and azimuth position $\theta$ of the primary rotor's upper and lower blades for standstill rotor at $U_\infty = 52.0 m/s$.*

# 5 Conclusions

The application of the 2D Actuator Cylinder model to the X-Rotor geometry resulted in a reasonably accurate simulation tool with a low computation cost, allowing the project to explore the design space. The aerodynamic model was used to compute the loads and performance of the rotor of the primary X-Rotor blades. The results are consistent with those of (Amiri & Carroll, 2021).

Wind tunnel data from a H-VAWT were used to validate the aeroelastic model. The MBD structural model is fast and accurate enough to model the mode shapes and effects observed or simulated with the higher fidelity model. The aerodynamic loading is effectively coupled in a one-way manner.

The model can support the X-Rotor project's immediate planned activities. As described in Task 2.1, the model will be further developed in the project, both as part of Task 2.1 and in conjunction with other tasks. The next steps include:

- Comparison with higher fidelity simulations.
- Implementation of the 3D Actuator Cylinder formulation, described in Section 2.
- Integration of higher fidelity sub-models, namely lifting line.
- Further exploration of the design space.
- Benchmark with other simulation tools.
- Simulation of the full X-Rotor, including secondary rotors.

# References


*AirfoilPrep.* (n.d.). https://www.nrel.gov/wind/nwtc/airfoil-prep.html.

Amiri, A. K., & Carroll, J. (2021). *X-rotor, an innovative offshore wind turbine. background and draft design* (Tech. Rep.). University of Strathclyde.

Drela, M. (1989). XFOIL: An Analysis and Design System for Low Reynolds Number Airfoils. In T. J. Mueller (Ed.), *Low Reynolds Number Aerodynamics* (pp. 1–12). Berlin, Heidelberg: Springer. doi: 10.1007/978-3-642-84010-4_1

Durand, W. F. (1935). *Aerodynamic Theory - Volume II Division E General Aerodynamic Theory*. Berlin: Springer. doi: 10.1007/978-3-642-91485-0

Ferreira, C. S., Madsen, H. A., Barone, M., Roscher, B., Deglaire, P., & Arduin, I. (2014, jun). Comparison of aerodynamic models for vertical axis wind turbines. *Journal of Physics: Conference Series*, *524*, 012125. Retrieved from https://doi.org/10.1088%2F1742-6596%2F524%2F1%2F012125 doi: 10.1088/1742-6596/524/1/012125

Glauert, H. (1948). *The elements of aerofoil and airscrew theory*. Cambridge University Press. doi: 10.1017CBO9780511574481

Keijer, W. (2020). *3d aerodynamic effects and circulation control of vertical axis wind turbines* (Master's thesis, Delft University of Technology, Technical University of Denmark, European Wind Energy Masters). Retrieved from http://resolver.tudelft.nl/uuid:765b00ba-7a80-4588-8476-774d7badc6cb

Larsen, T. J., & Madsen, H. A. (2013). On the way to reliable aeroelastic load simulation on vawt's. *European Wind Energy Conference and Exhibition, Ewec 2013*, *3*, 1721-1729.

LeBlanc, B., & Ferreira, C. (n.d.). Estimation of blade loads for a variable pitch vertical axis wind turbine from particle image velocimetry. *Wind Energy*, *n/a*(n/a). doi: 10.1002/we.2674

LeBlanc, B., & Ferreira, C. (2020, January). Experimental characterization of H-VAWT turbine for development of a digital twin. *Journal of Physics: Conference Series*, *1452*, 012057. doi: 10.1088/1742-6596/1452/1/012057

Leblanc, B., & Ferreira, C. (2020, September). Experimental Demonstration of Thrust Vectoring with a Vertical Axis Wind Turbine using Normal Load Measurements. *Journal of Physics: Conference Series*, *1618*, 052030. doi: 10.1088/1742-6596/1618/5/052030

LeBlanc, B., & Simao Ferreira, C. (2018, January). Overview and Design of PitchVAWT: Vertical Axis Wind Turbine with Active Variable Pitch for Experimental and Numerical Comparison. In *2018 Wind Energy Symposium.* Kissimmee, Florida: American Institute of Aeronautics and Astronautics. doi: 10.2514/6.2018-1243

LeBlanc, B. P., & Ferreira, C. S. (2018, June). Experimental Determination of Thrust Loading of a 2-Bladed Vertical Axis Wind Turbine. *Journal of Physics: Conference Series*, *1037*, 022043. doi: 10.1088/1742-6596/1037/2/022043

Leithead, W., Camciuc, A., Amiri, A. K., & Carroll, J. (2019, oct). The x-rotor offshore wind turbine concept. *Journal of Physics: Conference Series*, *1356*, 012031. Retrieved from https://doi.org/10.1088/1742-6596/1356/1/012031 doi: 10.1088/1742-6596/1356/1/012031

Madsen, H. A. (1983). *On the ideal and real energy conversion in a straight bladed vertical axis wind turbine* (PhD thesis). Aalborg University.

Madsen, H. A. (1988, November). Application of actuator surface theory on wind turbines. In *Iea r&d wecs: Joint action on aerodynamics of wind turbines.*

Madsen, H. A., Larsen, T. J., Schmidt Paulsen, U., & Vita, L. (2013). Implementation of the actuator cylinder flow model in the hawc2 code for aeroelastic simulations on vertical axis wind turbines. *Proceedings of 51st Aiaa Aerospace Sciences Meeting Including the New Horizons Forum and Aerospace Exposition*, 12 pp., 12 pp.

Simao Ferreira, C. (2009). *The near wake of the VAWT: 2d and 3d views of the VAWT aerodynamics* (Unpublished doctoral dissertation). Delft University of Technology. (ISBN/EAN:978-90-76468-14-3)

Simao Ferreira, C., & Scheurich, F. (2014). Demonstrating that power and instantaneous loads are decoupled in a vertical-axis wind turbine. *Wind Energy*, *17*(3), 385-396. Retrieved from https://onlinelibrary.wiley.com/doi/abs/10.1002/we.1581 doi: 10.1002/we.1581

van Kuik, G. (2018). *The fluid dynamic basis for actuator disc and rotor theories*. IOS Press. Retrieved from https://pure.tudelft.nl/portal/files/45541105/9781614998662.pdf

van Kuik, G. A. (2020). On the velocity at wind turbine and propeller actuator discs. *Wind Energy Science*, *5*(3), 855–865.

Viterna, L., & Janetzke, D. (1982, 10). Theoretical and experimental power from large horizontal-axis wind turbines. *NASA Technical Memorandum*.

# Appendix A - Definition of the output file with load distribution

This section presents the definition of the fields in the output files. The files are in a '.xls' (Excel file) format. The excel file has the following sheets:

- 'Simulation_properties'
- 'Blade_elements_description'
- 'Blade_elements_dimensions'
- 'Section_pitch_degrees'
- 'InflowAngle_degrees'
- 'NormalForce_N_per_m'
- 'TangentialForce_N_per_m'
- 'PitchingMoment_Nm_per_m'
- 'Local_performance'

### 0.0.1 Simulation_properties

This sheet presents the main properties that define the operational state of the simulation:

- **N Blades** the number of blades of the rotor
- **Radius (**$m$**)** the rotor radius in meters
- **Area (**$m^2$**)** the frontal area of the rotor in squared meters
- **Tip Speed ratio** the tip speed ratio, defined with the largest radius
- **Rotational speed (**$rad/s$**)** the rotational speed of the rotor in radians per second
- **Uinf (**$m/s$**)** the unperturbed wind speed in meters per second
- **Air density (**$kg/m^3$**)** the density of the air in kilograms per cubic meter
- **Power coefficient** the calculated power coefficient
- **Thrust coefficient** the calculated thrust coefficient
- **Power (**$MW$**)** the calculated power in megaWatts
- **Thrust (**$MN$**)** the calculated thrust in mega Newtons

### 0.0.2 Blade_elements_description

This sheet presents the description of each blade element. The first column indicates the index of the element (used in the next sheets). The second column indicates the name of the blade to which the element belongs **Blade name**. The third column indicates the airfoil polar used for the simulation of the performance of this element **Airfoil polar**.

*Table 5: Example of a "Simulation_properties" sheet.*

| | Value |
|---|---|
| N Blades | 2 |
| Radius ($m$) | 75 |
| Area ($m^2$) | 12870 |
| Tip Speed ratio | 3,787878788 |
| Rotational speed ($rad/s$) | 0,833333333 |
| Uinf ($m/s$) | 16,5 |
| Air density ($kg/m^3$) | 1,225 |
| Power coefficient | 0,203809091 |
| Thrust coefficient | 0,461810159 |
| Power ($MW$) | 7,217055176 |
| Thrust ($MN$) | 0,991096656 |

*Table 6: Example of a "Blade_elements_description" sheet.*

| | Blade name | Airfoil polar |
|---|---|---|
| 0 | BottomBlade | NACA0008_Re1p5e7n6.xls |
| 1 | BottomBlade | NACA0008_Re1p5e7n6.xls |
| 2 | BottomBlade | NACA0008_Re1p5e7n6.xls |
| 3 | BottomBlade | NACA0008_Re1p5e7n6.xls |
| ... | ... | ... |
| 66 | BottomBlade | NACA0025_Re1p5e7n6.xls |
| 67 | TopBlade | NACA0025_Re1p5e7n6.xls |
| 68 | TopBlade | NACA0025_Re1p5e7n6.xls |
| ... | ... | ... |
| 112 | TopBlade | NACA0012_Re1p5e7n6.xls |
| 113 | TopBlade | NACA0011_Re1p5e7n6.xls |

### 0.0.3 Blade_elements_dimensions

This sheet presents the dimensions and coordinates of each blade element.

- **Y mid-section (m)** Height of the mid-section of the blade element, in meters
- **X mid-section (m)** Radius of the mid-section of the blade element, in meters
- **Element length (m)** Length the blade element, in meters
- **Y start (m)** Height of the start-point of the blade element, in meters
- **Y end (m)** Height of the end-point of the blade element, in meters
- **X start (m)** Radius of the start-point of the blade element, in meters
- **X end (m)** Radius of the end-point of the blade element, in meters
- **chord (m)** Chord of the airfoil at midsection of the blade element, in meters
- **angle_to_normal (rad)** Angle of the blade element with the vertical, in radians

*Table 7: Example of a "Blade_elements_dimensions" sheet.*

| | Y mid-section (m) | X mid-section (m) | Element lentgh (m) | Y start (m) | Y end (m) | X start (m) | X end (m) | chord (m) | angle_to_normal (rad) |
|---|---|---|---|---|---|---|---|---|---|
| 0 | -42.022610 | 74.908088 | 0.240308 | -42.100000 | -41.945221 | 75.000000 | 74.816176 | 7.012868 | -0.870965 |
| 1 | -41.867831 | 74.724265 | 0.240308 | -41.945221 | -41.790441 | 74.816176 | 74.632353 | 7.038603 | -0.870965 |
| 2 | -41.713051 | 74.540441 | 0.240308 | -41.790441 | -41.635662 | 74.632353 | 74.448529 | 7.064338 | -0.870965 |
| 3 | -41.558272 | 74.356618 | 0.240308 | -41.635662 | -41.480882 | 74.448529 | 74.264706 | 7.090074 | -0.870965 |
| ... | ... | ... | | | | | | | |
| 137 | 85.804044 | 74.540441 | 0.367639 | 85.644853 | 85.963235 | 74.448529 | 74.632353 | 5.045956 | 0.523611 |
| 138 | 86.122426 | 74.724265 | 0.367639 | 85.963235 | 86.281618 | 74.632353 | 74.816176 | 5.027574 | 0.523611 |
| 139 | 86.440809 | 74.908088 | 0.367639 | 86.281618 | 86.600000 | 74.816176 | 75.000000 | 5.009191 | 0.523611 |

### 0.0.4 Section_pitch_degrees

This sheet presents the **Pitch Angle** (in degrees) of each blade element over the rotation and over the span of the blade. The first row indicates the mid-azimuthal position of blade (in degrees). The first column indicates the index of the blade element.

*Table 8: Example of a "Section_pitch_degrees" sheet.*

| | 4.00 | 12.00 | 20.00 | 28.00 | 36.00 | ... |
|---|---|---|---|---|---|---|
| 0 | .00 | .00 | 0.00 | .00 | .00 | ... |
| 1 | .00 | .00 | 0.00 | .00 | .00 | ... |
| 2 | .00 | .00 | 0.00 | .00 | .00 | ... |
| ... | ... | ... | | | | |
| 135 | 4.0 | 4.0 | 4.0 | 4.0 | 4.0 | ... |

### 0.0.5 InflowAngle_degrees

This sheet presents the **InflowAngle** (in degrees) at the midsection of each blade element over the rotation and over the span of the blade. The first row indicates the mid-azimuthal position of blade (in degrees). The first column indicates the index of the blade element.

*Table 9: Example of a "InflowAngle_degrees" sheet.*

| | 4.00 | 12.00 | 20.00 | 28.00 | 36.00 | ... |
|---|---|---|---|---|---|---|
| 0 | -0.675552 | 0.139366 | 0.951818 | 1.747079 | 2.513224 | ... |
| 1 | -0.680566 | 0.135612 | 0.949473 | 1.746216 | 2.513877 | ... |
| ... | ... | ... | | | | |
| 87 | -2.772872 | -1.101471 | 0.636292 | 2.403248 | 4.174838 | ... |
| ... | ... | ... | | | | |
| 131 | -1.394762 | -0.291046 | 0.814393 | 1.901326 | 2.952755 | ... |

### 0.0.6 NormalForce_N_per_m

This sheet presents the **Normal Force** (force perpendicular to the actuation surface, understood as perpendicular to the azimuthal and spanwise direction) per unit length of the element (Newton per meter) at the midsection of each blade element over the rotation and over the span of the blade. The first row indicates the mid-azimuthal position of blade (in degrees). The first column indicates the index of the blade element.

*Table 10: Example of a "NormalForce_N_per_m" sheet.*

| | 4.00 | 12.00 | 20.00 | 28.00 | 36.00 | ... |
|---|---|---|---|---|---|---|
| 0 | -1190.260186 | 243.039634 | 1636.562112 | 2943.739568 | 4129.597369 | ... |
| 1 | -1198.808029 | 236.417808 | 1631.929922 | 2941.012931 | 4128.589977 | ... |
| ... | ... | ... | | | | |
| 49 | -2553.770470 | -1207.536734 | 163.867781 | 1468.261651 | 2643.092561 | ... |
| ... | ... | ... | | | | |
| 125 | 3321.541220 | 4654.662009 | 5914.805860 | 7059.191088 | 8052.086383 | ... |

### 0.0.7 TangentialForce_N_per_m

This sheet presents the **Tangential Force** (force in azimuthal direction) per unit length of the element (Newton per meter) at the midsection of each blade element over the rotation and over the span of the blade. The first row indicates the mid-azimuthal position of blade (in degrees). The first column indicates the index of the blade element.

*Table 11: Example of a "TangentialForce_N_per_m" sheet.*

| | 4.00 | 12.00 | 20.00 | 28.00 | 36.00 | ... |
|---|---|---|---|---|---|---|
| 0 | -69.557216 | -81.868997 | -54.687741 | 8.656466 | 100.705104 | ... |
| 1 | -69.333215 | -81.868749 | -54.797492 | 8.566056 | 100.747028 | ... |
| ... | ... | ... | | | | |
| 49 | 33.861916 | -38.792350 | -58.327567 | -20.267218 | 69.984147 | ... |
| ... | ... | ... | | | | |
| 125 | -132.595946 | -69.722331 | 44.625772 | 202.340801 | 390.806177 | ... |

### 0.0.8 PitchingMoment_Nm_per_m

This sheet presents the **Pitching/torsional moment** moment per unit length of the element (Newton.meter per meter) at the midsection of each blade element over the rotation and over the span of the blade. The first row indicates the mid-azimuthal position of blade (in degrees). The first column indicates the index of the blade element.

*Table 12: Example of a "PitchingMoment_Nm_per_m" sheet.*

| | 4.00 | 12.00 | 20.00 | 28.00 | 36.00 | ... |
|---|---|---|---|---|---|---|
| 0 | 2.193868e+01 | 0.000000 | -29.524395 | -49.668557 | -6.716781e+01 | ... |
| 1 | 2.201332e+01 | 0.000000 | -29.495889 | -49.783804 | -6.741390e+01 | ... |
| ... | ... | ... | | | | |
| 49 | 1.004010e+02 | 53.023904 | -17.355066 | -66.656409 | -1.052647e+02 | ... |
| ... | ... | ... | | | | |
| 125 | -4.362086e+01 | -58.352583 | -66.830169 | -69.529413 | -6.620256e+01 | ... |

### 0.0.9 Local_performance

This sheet presents the area and key performance parameters ($C_P$,$C_T$) for the rotor area swept by each blade element. $C_P$ and $C_T$ are determined with the local area.

*Table 13: Example of a "Local_performance" sheet.*

| | Area covered by blade section | CP local | CT local |
|---|---|---|---|
| 0 | 23.188460 | 0.400103 | 0.686995 |
| 1 | 23.131555 | 0.400759 | 0.688488 |
| 2 | 23.074651 | 0.401411 | 0.689976 |
| 3 | 23.017747 | 0.402056 | 0.691459 |
| ... | ... | ... | |
| 87 | 134.844291 | 0.533904 | 0.859923 |
| 88 | 138.173779 | 0.533167 | 0.859462 |
| ... | ... | ... | |
| 137 | 47.464722 | 0.273073 | 0.507435 |
| 138 | 47.581774 | 0.246011 | 0.475920 |
| 139 | 47.698827 | 0.192453 | 0.407142 |

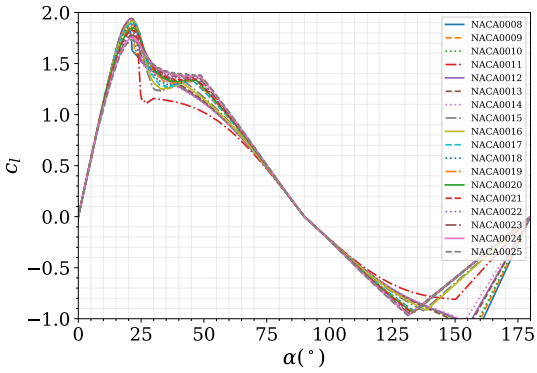


*(a) $c_l$ as function of $\alpha$ for several airfoils, $Re = 1.5e+7$ and transition amplification factor $n = 6$.*

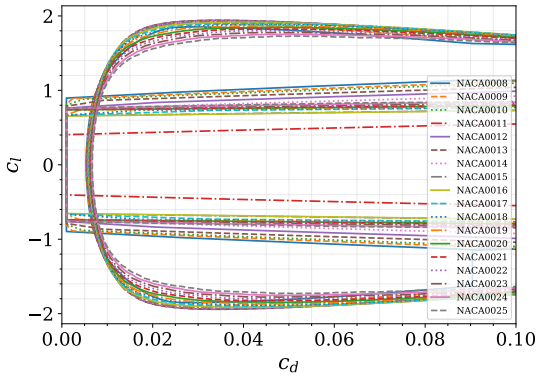


*(b) $c_l$ as function of $c_D$ for several airfoils, $Re = 1.5e+7$ and transition amplification factor $n = 6$.*

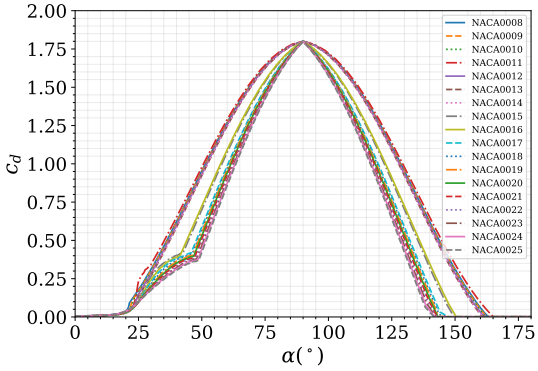


*(c) $c_d$ as function of $\alpha$ for several airfoils, $Re = 1.5e+7$ and transition amplification factor $n = 6$.*

*Figure 19: Polars used in the simulations.*

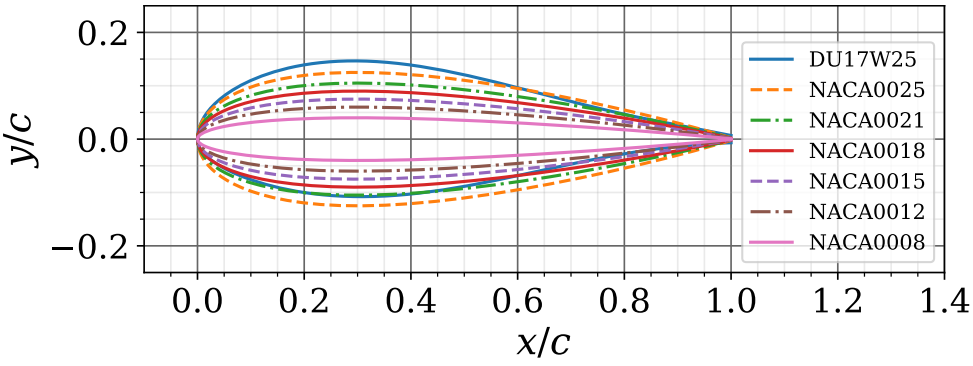


*Figure 20: Geometry of the airfoils non-dimensioned by chord $c$.*

# Appendix B - Airfoil polars

All airfoil polars were calculated using XFOIL (Drela, 1989) for a Reynolds number of $1.5 * 10^7$ and free transition, with the criteria for transition set at $n = 6$. All polars are available in the data sub-folder *"Polars"*. The polars are extended to $\alpha = [-180..180]$ using the method by (Viterna & Janetzke, 1982) as implemented in *Airfoilprep* (*AirfoilPrep*, n.d.)

Figure 19 presents the polars used in the simulation. Figure 20 shows the airfoil geometry for several of the airfoils.

## Consortium

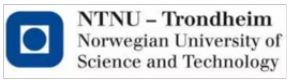

## Disclaimer

All information provided reflects the status of the XROTOR project at the time of writing and may be subject to change.

Neither the XROTOR Consortium as a whole, nor any single party within the XROTOR Consortium warrant that the information contained in this document is capable of use, nor that the use of such information is free from risk. Neither the XROTOR Consortium as a whole, nor any single party within the XROTOR Consortium accepts any liability for loss or damage suffered by any person using the information.

This document does not represent the opinion of the European Community, and the European Community is not responsible for any use that might be made of its content.

## Copyright Notice